Cosmology from cross-correlation of ACT-DR4 CMB lensing and DES-Y3 cosmic shear

S. Shaikh [1]★ I. Harrison,[2]★ A. van Engelen,[1] G. A. Marques,[3,4] T. M. C. Abbott,[5] M. Aguena [6]
O. Alves,[7] A. Amon,[8,9] R. An,[10] D. Bacon,[11] N. Battaglia,[12] M. R. Becker,[13] G. M. Bernstein,[14]
E. Bertin,[15,16] J. Blazek,[17] J. R. Bond,[18] D. Brooks,[19] D. L. Burke,[20,21] E. Calabrese,[2]
A. Carnero Rosell,[6,22,23] J. Carretero,[24] R. Cawthon,[25] C. Chang,[4,26] R. Chen,[27] A. Choi,[28] S. K. Choi,[12,29]
L. N. da Costa,[6] M. E. S. Pereira,[30] O. Darwish,[31] T. M. Davis,[32] S. Desai,[33] M. Devlin,[14] H. T. Diehl,[3]
P. Doel,[19] C. Doux,[14,34] J. Elvin-Poole,[35] G. S. Farren,[9,36] S. Ferraro,[37,38] I. Ferrero,[39] A. Ferté,[21]
B. Flaugher,[3] J. Frieman,[3,4] J. García-Bellido,[40] M. Gatti,[14] G. Giannini,[24] S. Giardiello,[2] D. Gruen,[41]
R. A. Gruendl,[42,43] G. Gutierrez,[3] J. C. Hill,[44] S. R. Hinton,[32] D. L. Hollowood,[45] K. Honscheid,[46,47]
K. M. Huffenberger,[48] D. Huterer,[7] D. J. James,[49] M. Jarvis,[14] N. Jeffrey,[19] H. T. Jense,[2] K. Knowles,[50,51]
J. Kim,[14] D. Kramer,[1] O. Lahav,[19] S. Lee,[52] M. Lima,[6,53] N. MacCrann,[36] M. S. Madhavacheril,[14]
J. L. Marshall,[54] J. McCullough,[20] Y. Mehta,[1] J. Mena-Fernández,[55] R. Miquel,[24,56] J. J. Mohr,[41,57]
K. Moodley,[58,59] J. Myles,[20,21,60] A. Navarro-Alsina,[61] L. Newburgh,[62] M. D. Niemack,[12,29]
Y. Omori,[4,20,26,60] S. Pandey,[14] B. Partridge,[63] A. Pieres,[6,64] A. A. Plazas Malagón,[20,21] A. Porredon,[46,47,65]
J. Prat,[4,26] F. J. Qu,[9,36] N. Robertson,[65] R. P. Rollins,[65] A. Roodman,[20,21] S. Samuroff,[17] C. Sánchez,[14]
E. Sanchez,[55] D. Sanchez Cid,[55] L. F. Secco,[4] N. Sehgal,[66] E. Sheldon,[67] B. D. Sherwin,[9,36] T. Shin,[66]
C. Sifón,[68] M. Smith,[69] E. Suchyta,[70] M. E. C. Swanson,[42] G. Tarle,[7] M. A. Troxel,[27] I. Tutusaus,[71]
C. Vargas,[72] N. Weaverdyck,[7,37] P. Wiseman,[69] M. Yamamoto,[27] and J. Zuntz[65] (The ACT and DES Collaborations)

Affiliations are listed at the end of the paper

ABSTRACT

Cross-correlation between weak lensing of the Cosmic Microwave Background (CMB) and weak lensing of galaxies offers a way to place robust constraints on cosmological and astrophysical parameters with reduced sensitivity to certain systematic effects affecting individual surveys. We measure the angular cross-power spectrum between the Atacama Cosmology Telescope (ACT) DR4 CMB lensing and the galaxy weak lensing measured by the Dark Energy Survey (DES) Y3 data. Our baseline analysis uses the CMB convergence map derived from ACT-DR4 and *Planck* data, where most of the contamination due to the thermal Sunyaev Zel'dovich effect is removed, thus avoiding important systematics in the cross-correlation. In our modelling, we consider the nuisance parameters of the photometric uncertainty, multiplicative shear bias and intrinsic alignment of galaxies. The resulting cross-power spectrum has a signal-to-noise ratio = 7.1 and passes a set of null tests. We use it to infer the amplitude of the fluctuations in the matter distribution ($S_8 \equiv \sigma_8(\Omega_{\mathrm{m}}/0.3)^{0.5} = 0.782 \pm 0.059$) with informative but well-motivated priors on the nuisance parameters. We also investigate the validity of these priors by significantly relaxing them and checking the consistency of the resulting posteriors, finding them consistent, albeit only with relatively weak constraints. This cross-correlation measurement will improve significantly with the new ACT-DR6 lensing map and form a key component of the joint $6{\times}2$pt analysis between DES and ACT.

Key words: gravitational lensing: weak – large-scale structure of Universe – cosmology: observations – cosmological parameters.

1 INTRODUCTION

Observations of the $z \sim 1100$ Cosmic Microwave Background (CMB) and the Large-Scale Structure (LSS) at $z \lesssim 3$ give a remark-

★ E-mail: sshaik14@asu.edu (SS); harrisoni@cardiff.ac.uk (IH)

ably consistent picture of the physics and contents of the universe. Measurements of the primary CMB temperature and polarization anisotropies from *Planck* 2018 (Planck Collaboration 2020), ACT Data Release 4 (DR4) (Aiola et al. 2020) and SPT-3G (Dutcher et al. 2021) achieve sub-per cent precision on the six main parameters of the spatially flat Lambda Cold Dark Matter (ΛCDM) cosmological model. This model allows us to predict several derived parameters, which can be measured using different probes at lower redshifts. One such derived parameter is the matter clustering parameter σ_8, which describes the amplitude of fluctuations in the overdensity of matter on scales of $8\,h^{-1}$ Mpc. Large photometric and spectroscopic surveys of galaxies have recently begun to place constraints on this parameter comparable in precision to those obtained from CMB predictions. The most recent results from the Dark Energy Survey (DES-Y3, Abbott et al. 2022), the Kilo-Degree Survey (KiDS-1000, Heymans et al. 2021) and the Hyper-Suprime Cam survey (HSC-Y3, Miyatake et al. 2023; More et al. 2023; Sugiyama et al. 2023) all combine galaxy clustering and galaxy weak lensing measurements to infer the value of σ_8 and the total matter abundance Ω_m, with the best-constrained parameter combination given by $S_8 \equiv \sigma_8(\Omega_m/0.3)^{0.5}$.

As the statistical uncertainty from these two different sets of experiments shrank, a discrepancy emerged: high redshift CMB observations favour a value scattering around $S_8 \approx 0.83$ (ACT-DR4: 0.830 ± 0.043; *Planck* PR3: 0.834 ± 0.016; SPT-3G 2018: 0.797 ± 0.041), whilst low redshift galaxy and lensing observations appear close to a lower value of $S_8 \approx 0.77$ (DES-Y3: 0.776 ± 0.017; KiDS-1000: $0.766^{+0.020}_{-0.014}$, HSC-Y3: $0.775^{+0.043}_{-0.038}$). This disagreement is marginally statistically significant but remains consistent when comparing different experiments (see Abdalla et al. 2022, for a review; here, we attempt to include a representative sub-sample of the latest results). This disagreement could be due to unaccounted-for systematics in one (or both) types of experiment or due to a missing piece of physics affecting structure growth at different redshifts and/or physical scales. The prospect of modifications to the current understanding of non-linear structure formation and baryonic feedback contributions is pointed to by Amon et al. (2023), Amon & Efstathiou (2022), Gu et al. (2023) and references therein. A number of other explanations include new dark sector physics, including interacting dark energy and dark matter (e.g. Poulin et al. 2023), and ultra-light axions (e.g. Rogers et al. 2023).

Along with these two principal probes, several other probes are sensitive to an intermediate range of redshifts. Gravitational lensing of the primary CMB is sensitive to a broad range of redshifts and large angular scales. It agrees largely on the value of S_8 with the primary CMB itself: the latest ACT results from the newly produced DR6 lensing map (MacCrann et al. 2023; Madhavacheril et al. 2023; Qu et al. 2023) find $S_8 = 0.840 \pm 0.028$. Cross-correlations of this CMB lensing signal with galaxy surveys are beginning to be detected at increasing signal-to-noise, hence their ability to provide useful constraints. These cross-correlations are sensitive to lower redshifts and smaller scales compared to the CMB lensing autospectrum and generally prefer values of $S_8 < 0.8$, in agreement with the galaxy clustering and weak lensing measurements (e.g. Robertson et al. 2021: 0.64 ± 0.08, Krolewski, Ferraro & White 2021: 0.784 ± 0.015, Chang et al. 2023: $0.74^{+0.034}_{-0.029}$, Marques et al. 2023: $0.75^{+0.04}_{-0.05}$.).

Here, we focus specifically on one of these cross-correlations: the one between CMB lensing (κ_C) and galaxy weak lensing (γ_E), which we will refer to as $C_\ell^{\kappa_C \gamma_E}$. To measure this, we use a combination of the ACT-DR4 CMB lensing map (Darwish et al. 2021) and the DES-Y3 galaxy shape catalogue (Gatti et al. 2021). The cross-correlation lensing kernel peaks between those of each probe individually (see lower panel of Fig. 1) and hence probes somewhat different redshift
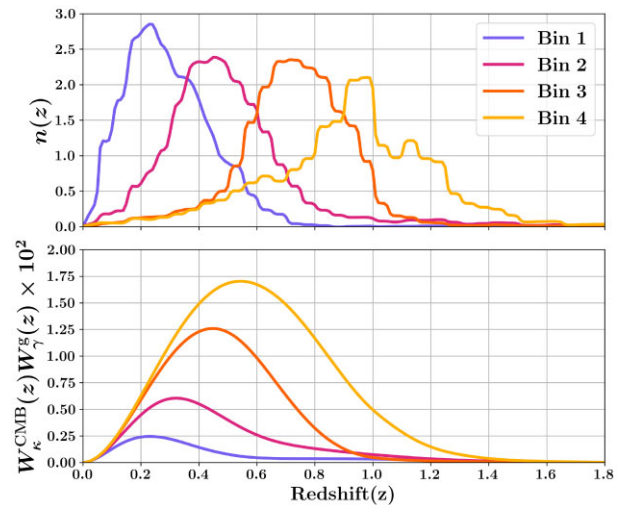

Figure 1. Top panel shows the DES-Y3 source galaxy redshift distribution, $n(z)$, in four tomographic bins. The bottom panel shows the product of the respective galaxy weak lensing kernel with the CMB weak lensing kernel.

range than the galaxy weak lensing alone. CMB lensing–galaxy weak lensing cross-correlations are not sensitive to galaxy bias and also provide useful information on the systematics of both probes. Specifically, the extra high-redshift lensing bin from the CMB has long been proposed as a useful way of calibrating multiplicative biases in the difficult measurement of galaxy lensing shear and shift biases in the estimated mean photometric redshift of the galaxy samples (e.g. Das, Errard & Spergel 2013).

A number of analyses have already detected this cross-correlation signal (Hand et al. 2015; Liu & Hill 2015; Harnois-Déraps et al. 2016; Kirk et al. 2016; Harnois-Déraps et al. 2017; Singh, Mandelbaum & Brownstein 2017; Omori et al. 2019; Marques et al. 2020; Robertson et al. 2021; Chang et al. 2023). Some of these early works focus the signal-to-noise available from their data onto a single phenomenological parameter A_{cross}, which is the amplitude of the cross-correlation power spectrum relative to that predicted by primary CMB data. Note that we denote this parameter by A_{cross} to distinguish it from the parameter measuring the smearing of the peaks in the primary CMB power spectrum, A_{lens}, as introduced in Calabrese et al. (2008). Robertson et al. (2021) also explicitly measure S_8 jointly with other cosmological and systematics parameters, finding a 1D marginalized constraint of $S_8 = 0.64 \pm 0.08$, which is consistent with low redshift weak lensing only constraints but inconsistent with results derived from high redshift CMB measurements. Omori et al. (2023) and Chang et al. (2023) measure the real-space equivalents of the $C_\ell^{\kappa_C \gamma_E}$ data vector and the CMB lensing–galaxy clustering cross-correlation between SPT and DES-Y3, finding $S_8 = 0.74^{+0.034}_{-0.029}$. They then combine these cross-correlations with the three DES-Y3 data vectors and one SPT lensing data vector for a full '6×2pt'.[1] analysis using information from this wide range of kernels spanning a large range of redshifts, finding $S_8 = 0.792 \pm 0.012$ (Abbott et al. 2023).

In addition, Robertson et al. (2021) and Marques et al. (2020) also assess the consistency of their $C_\ell^{\kappa_C \gamma_E}$ only data with the priors on multiplicative shear and redshift calibration biases, which are derived by the weak lensing experiments using a combination of

---

[1]So called because it involves six combinations of the two-point correlation functions of CMB lensing κ, galaxy lensing γ and galaxy positions g: $\langle \kappa\kappa \rangle$, $\langle \gamma\gamma \rangle$, $\langle gg \rangle$, $\langle \kappa\gamma \rangle$, $\langle \kappa g \rangle$, $\langle \gamma g \rangle$.

simulations and deep ancillary observational data. For these two types of parameters, there is very little constraining power available from current $C_\ell^{\kappa_C \gamma_E}$ data, but the results are indeed consistent with the priors derived without the assistance of the high redshift CMB lensing bin (which is independent of the calibration parameters).

Another physical effect that affects the amplitude of the $C_\ell^{\kappa_C \gamma_E}$ signal is the intrinsic alignment of galaxies (IA), which can mimic the alignment caused by the weak lensing cosmic shear signal (for a review see Troxel & Ishak 2015). The amplitude of the power spectrum of IAs is highly degenerate with the lensing amplitude and forms a contribution to the observed power spectrum of $\mathcal{O}(10$ per cent) (Hall & Taylor 2014). Models for the power spectrum of IAs motivated by galaxy formation physics are relatively uncertain but are expected to have redshift and scale dependencies which help to break this degeneracy (Vlah, Chisari & Schmidt 2020, and references therein).

With 450 deg^2 of overlapping ACT-DR4 and DES-Y3 data, we have the necessary ingredients to perform a full tomographic analysis using the four redshift bins defined by DES-Y3. We include a set of four redshift calibration parameters, four shear calibration parameters, and two parameters describing the IA amplitude and redshift dependence. The current signal-to-noise from the ACT-DR4 and DES-Y3 allows us to put constraints on S_8 from $\kappa_C \gamma_E$ which, although weaker than those of Abbott et al. (2023) (primarily due to a smaller available overlapping sky area) provides an opportunity to favour or disfavour the somewhat inconsistent values for S_8 from $C_\ell^{\kappa_C \gamma_E}$ currently found in the literature. Furthermore, we are careful to ensure our methods are adequate for the incoming three-fold increase in constraining power available from the ACT-DR6 lensing map relative to ACT-DR4. The ACT-DR6 lensing map covers most of the DES survey footprint, allowing for a factor of ≈ 9 increase in the area of overlap between the two surveys, compared to the ACT-DR4 lensing map considered in this work. This will bring our constraining power up to a level comparable to the best current measurements of $C_\ell^{\kappa_C \gamma_E}$ from Chang et al. (2023). Our analysis is performed in harmonic space, rather than real space as in that work, and thus has different sensitivity to behaviour at different redshifts and scales, and may thus provide useful verification of earlier results.

We have structured the paper in the following manner:

(i) In Section 2, we describe the theory predicting our observable: the angular cross-power spectrum between CMB weak lensing and galaxy weak lensing.

(ii) In Section 3, we briefly describe the overall features of the ACT and DES surveys. We discuss the ACT-DR4 lensing map and DES-Y3 cosmic shear catalogue, which we use as inputs to our analysis.

(iii) In Section 4, we describe cross-power spectrum estimation from these inputs, including the generation of the simulations we use for pipeline validation and estimating the covariance matrix for the data.

(iv) In Section 5, we describe the framework in which we compare the data vector to theory predictions, including the parametrization of the cosmological model and galaxy weak lensing nuisance model. We also describe our inference pipeline in terms of likelihood, prior, and sampling methodology choices.

(v) In Section 6, we describe the validation of this pipeline. We conduct a series of null tests on the blinded data vector to ensure there is no significant detectable contamination from unmodelled observational and astrophysical effects. We also inject simulated data into our inference pipeline and show we can recover the input model parameters in an unbiased way. We demonstrate the stability of our

measurement of the cosmological parameters to different choices of the underlying modelling and splitting our data vector into sub-samples in a number of ways.

(vi) In Section 7, we show our constraints on cosmological and weak lensing galaxy nuisance parameters. We first infer the value of the lensing amplitude A_{cross} with respect to the prediction from a standard ΛCDM cosmology. We then show our measurement of the parameters in the full model, including cosmology and galaxy weak lensing nuisance parameters. We also explore our constraining power on the nuisance parameters when DES simulation- and deep data-derived priors are relaxed and when using only high- and low-redshift sub-samples of our data.

(vii) In Section 8, we review our conclusions and discuss their implications.

2 THEORY

Gravitational lensing of the light from cosmic sources such as the CMB and galaxies allows us to probe the distribution of matter intervening between these sources and the observer. Weak-lensing convergence (κ) is the weighted integral of the matter density contrast $\delta(z, \hat{n})$ (e.g. Schneider 2005, and references therein)

$$\kappa(\hat{n}) = \int W(z)\delta(z, \hat{n})dz, \tag{1}$$

where $W(z)$ is the lensing weight as a function of redshift and $\hat{n}$ is the direction on the sky. $W(z)$ represents the lensing efficiency of the matter distribution along the line of sight. Weak-lensing shear (γ), which is a spin-2 quantity with two components, (γ_1, γ_2). In harmonic space, the spin-2 field is described by E and B mode harmonic coefficients:

$$\gamma_1(\hat{n}) \pm i\gamma_2(\hat{n}) = \sum_{\ell m} \left(\gamma_{\ell m}^E \pm i\gamma_{\ell m}^B\right) {}_{\pm 2}Y_{\ell m}(\hat{n}), \tag{2}$$

where ${}_{\pm 2}Y_{\ell m}(\hat{n})$ are spin-2 spherical harmonics and $\gamma_{\ell m}^E$ and $\gamma_{\ell m}^B$ are the spherical harmonic coefficients of E and B modes of the shear field (e.g. Castro, Heavens & Kitching 2005). At linear order in deflection, weak lensing by LSS only contributes to the E-mode signal in the shear, which is related to κ through the following harmonic space relation

$$\gamma_{\ell m}^E = -\sqrt{\frac{(\ell - 1)(\ell + 2)}{\ell(\ell + 1)}} \kappa_{\ell m}, \tag{3}$$

where $\kappa_{\ell m}$ are spherical harmonic coefficients of κ. This work uses the correlation between the convergence reconstructed from the observed CMB (κ_C) and the weak lensing shear measured by galaxy imaging surveys (γ). κ_C is reconstructed from the observed CMB maps using quadratic estimators (Darwish et al. 2021), whereas γ is estimated from the measurement of galaxy ellipticities $e \equiv (e_1, e_2)$, with e_1 and e_2 being two components of the galaxy ellipticities (Gatti et al. 2021). Even though, in principle, shear can be estimated from a simple average of ellipticities, DES-Y3 analysis uses the METACALIBRATION method (Huff & Mandelbaum 2017):

$$\langle \gamma \rangle \approx \langle \mathbf{R} \rangle^{-1} \langle e \rangle, \tag{4}$$

where the matrix $\mathbf{R}$ is the shear response for the galaxies, measured by repeating the ellipticity measurement on sheared versions of the galaxy images:

$$R_{i,j} = \frac{e_i^+ - e_i^-}{\Delta\gamma_j}, \tag{5}$$

where $e^{\pm}$ is the measurement on an image sheared by a small amount $\pm\gamma$ and $\Delta\gamma = 2\gamma$.

We model the correlation between κ_C and γ_E in spherical harmonic space. The angular power spectrum between the CMB convergence κ_C and the E-mode of the galaxy shear γ_E at multipole ℓ, under the Limber approximation (Limber 1953; LoVerde & Afshordi 2008), is (e.g. Kaiser 1992)

$$C_\ell^{\kappa_C \gamma_E} = \int_0^{z_H} dz \frac{H(z)}{\chi^2(z)c} W_\kappa^{CMB}(z) W_\gamma^g(z) P_{\delta\delta}\left(k = \frac{\ell + 0.5}{\chi(z)}, z\right), \quad (6)$$

where $P_{\delta\delta}(k, z)$ is the matter power spectrum at redshift z, $\chi(z)$, and $a(z)$ denote the co-moving distance and the scale factor at z, respectively, c is the speed of light, and $H(z)$ is the Hubble parameter as a function of z. $W_\kappa^{CMB}(z)$ and $W_\gamma^g(z)$ are the lensing weights for the CMB and the source galaxies, respectively. The lensing weight for the CMB is given by

$$W_\kappa^{CMB}(z) = \frac{3 H_0^2 \Omega_{m,0}}{2 H(z) c} \frac{\chi(z)}{a(z)} \frac{\chi(z^*) - \chi(z)}{\chi(z^*)}, \quad (7)$$

where z^* is the redshift of the surface of the last scattering of the CMB, $\Omega_{m,0}$, and H_0 are matter density and Hubble parameters at the current epoch. The lensing weight for the source galaxies depends on their redshift distribution, $n(z)$:

$$W_\gamma^g(z) = \frac{3 H_0^2 \Omega_{m,0}}{2 H(z) c} \frac{\chi(z)}{a(z)} \int_z^{z_H} dz' n(z') \frac{\chi(z') - \chi(z)}{\chi(z')}. \quad (8)$$

We use the Core Cosmology Library (CCL, Chisari et al. 2019) to compute $C_\ell^{\kappa_C \gamma_E}$.[2] We model the non-linear contributions to $P_{\delta\delta}(k)$ using the halofit model (Smith et al. 2003; Takahashi et al. 2012). We also include contributions to the observed power spectrum from astrophysical and experimental effects, which we fully describe in Section 5.2.

In Fig. 1, we show the source redshift distribution $n(z)$ used in this work and the product of the lensing weight function $W_\kappa^{CMB}(z) W_\gamma^g(z)$. The latter shows the redshift range of the matter distribution that contributes to the cross-correlation $C_\ell^{\kappa_C \gamma_E}$.

3 DATA

We use overlapping CMB weak lensing and galaxy weak lensing data from the ACT and DES, respectively. We extensively use the individual work of these collaborations in reducing their raw data and preparing science-ready CMB lensing maps and cosmic shear catalogues, but we perform our own analyses to generate the cross-correlation $C_\ell^{\kappa_C \gamma_E}$ data vector.

3.1 ACT CMB lensing data

We use the ACT-DR4 CMB lensing convergence maps from Darwish et al. (2021). These lensing maps are reconstructed using CMB temperature and polarization measurements by ACT in two frequency channels (98 and 150 GHz) during the 2014 and 2015 observing seasons (Aiola et al. 2020; Mallaby-Kay et al. 2021). The arcminute-resolution maps produced by the ACT Collaboration are described in Aiola et al. (2020); Choi et al. (2020); Madhavacheril et al. (2020). ACT-DR4 consists of lensing maps in two sky regions, Deep-56 (D56) and BOSS-North (BN), with respective sky areas 456 deg² and 1633 deg² (Darwish et al. 2021). We use the lensing map in the D56 region, which overlaps with the DES-Y3 footprint, as shown in Fig. 2.
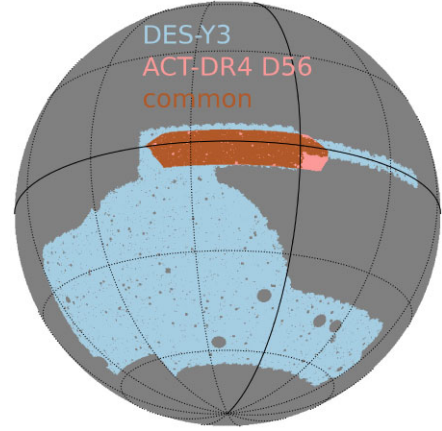
[2]https://github.com/LSSTDESC/CCL

Figure 2. DES-Y3 and ACT-DR4 D56 footprints and their common footprint. The sky area common between them is around 450 deg².

CMB lensing maps are obtained using the quadratic estimator (Hu & Okamoto 2002). Signatures of extragalactic astrophysical processes present in the individual frequency maps, such as the Cosmic Infrared Background (CIB) and thermal Sunyaev–Zeldovich (tSZ) effect, lead to biases in the reconstructed convergence map (Osborne, Hanson & Doré 2014; van Engelen et al. 2014). These signals trace the LSS and can lead to biases in the cross-correlation of κ_C with other LSS probes, such as galaxy weak lensing. For the range of redshifts ($z \lesssim 1.0$) probed by ACT-DR4 and DES-Y3 $C_\ell^{\kappa_C \gamma_E}$, the biases due to tSZ are expected to be more prominent than those due to the CIB (Baxter et al. 2019), which is sourced by galaxies spanning a broad range of redshift with the peak between $z \sim 1$ to 2 (Schmidt et al. 2015). ACT-DR4 provides two lensing maps: a tSZ-free κ_C map where the contamination due to the tSZ effect is deprojected (Madhavacheril & Hill 2018), and with-tSZ κ_C map where the tSZ deprojection is not performed. We refer to results obtained using this latter map as 'ACT-only'. The tSZ-free κ_C map uses *Planck* frequency maps along with the ACT data to perform the internal linear combination step required to deproject tSZ contamination and obtain the tSZ-free CMB map (Madhavacheril & Hill 2018; Madhavacheril et al. 2020). Hence, we refer to results derived from this map as 'ACT+*Planck*'. In the ACT-DR4 analysis, the CMB lensing maps are reconstructed using Fourier modes between ℓ_{min}^{CMB} and ℓ_{max}^{CMB}. The lower multipole, ℓ_{min}^{CMB}, is chosen to mitigate the effects of the atmospheric noise and the ACT mapmaker transfer function (Darwish et al. 2021). ℓ_{max}^{CMB} is chosen to avoid contamination due to extragalactic foregrounds. The ACT-only convergence map is reconstructed with $\ell_{min}^{CMB} = 500$ and $\ell_{max}^{CMB} = 3000$. The tSZ-cleaned CMB map obtained using *Planck* frequency maps contains information on large angular scales, below $\ell < 500$. Hence, using ACT+*Planck* data and tSZ deprojection makes a wider range of CMB multipoles suitable for lensing reconstruction with $\ell_{min}^{CMB} = 100$ and $\ell_{max}^{CMB} = 3350$. In Fig. 3, we show the ACT+*Planck* κ_C map over the D56 region. This map is smoothed using a Gaussian kernel of 12 arcmin FWHM for visual purposes only. We use the κ_C map without any additional smoothing in the analysis.

ACT lensing reconstruction is performed using a lensing analysis mask applied to the individual frequency maps or CMB maps. While computing the angular power spectrum, we use the square of this mask as the mask implicit in the reconstructed κ_C map. We also use 511 lensing reconstruction simulations made available by Darwish et al. (2021) to obtain the lensing reconstruction noise.
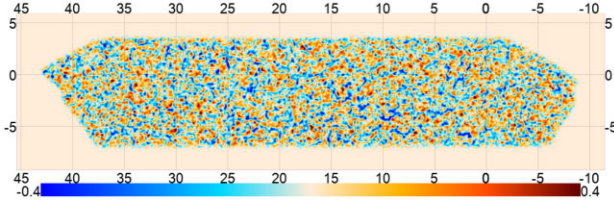
Figure 3. ACT-DR4 κ_C map reconstructed using ACT and *Planck* data in the D56 region. The map shown here is smoothed with a Gaussian kernel of 12 arcmin FWHM for visual purposes. The *x*-axis indicates right ascension, and the y-axis indicates declination.

Table 1. Summary of source galaxy catalogue. $z_1^{PZ} - z_2^{PZ}$ is the range of photometric redshifts of the given tomographic bin (Myles et al. 2021), n_{eff} is the effective number density of source galaxies in units of gal/arcmin^2, and σ_e is uncertainty in the measurement of one component of the shape (Amon et al. 2022). $\bar{R}_1$ and $\bar{R}_2$ are the average METACALIBRATION responses for two galaxy ellipticity components (Gatti et al. 2021).

Redshift bin	Bin-1	Bin-2	Bin-3	Bin-4
$z_1^{PZ} - z_2^{PZ}$	0.0–0.36	0.36–0.63	0.63–0.87	0.87–2.0
n_{eff}	1.476	1.479	1.484	1.461
σ_e	0.243	0.262	0.259	0.310
$\bar{R}_1$	0.767	0.726	0.701	0.629
$\bar{R}_2$	0.769	0.727	0.702	0.630

The ACT κ_C maps are in the equirectangular plate carree (CAR) projection. We use the `pixell` package to convert the maps from CAR projection to the `HEALPix` pixelization at resolution `Nside` = 2048 (Górski et al. 2005).[3]

3.2 DES-Y3 galaxy weak lensing data

DES is a photometric survey that carried out observations using the Dark Energy Camera (Flaugher et al. 2015) on Cerro Tololo Inter-American Observatory (CTIO) Blanco 4-m Telescope in Chile. We use the weak lensing source galaxies catalogue of the DES-Y3 data. The catalogue is derived from the DES-Y3 GOLD data products (Sevilla-Noarbe et al. 2021). The shape measurement of source galaxies is performed using the METACALIBRATION algorithm (Huff & Mandelbaum 2017; Sheldon & Huff 2017) and is discussed in Gatti et al. (2021). After various selection cuts are applied to reduce systematic biases, the catalogue contains the shape measurement (e_1, e_2) of $\sim 1 \times 10^8$ galaxies. It spans an effective (unmasked) area of 4143 deg^2 with effective number density n_{eff} = 5.59 gal/arcmin^2.

The galaxies in the source catalogue are distributed in four tomographic redshift bins shown in Fig. 1. Photometric redshifts of these galaxies are estimated using the SOMPZ algorithm (Myles et al. 2021) using deep observations and additional colour bands from the DES deep fields (Hartley et al. 2022). The effective number of sources and the uncertainty in one component of the ellipticity measurement (σ_e) for each redshift bin are shown in Table 1.

The catalogue provides the inverse variance weight (w) for the shape measurement of each galaxy. When computing the angular power spectrum, we use these weights to form the mask to be applied to the shear maps. We use the sum-of-weights scheme discussed in Nicola et al. (2021) to prepare this mask. We discuss this procedure in Section 4.2.

[3]https://github.com/simonsobs/pixell

3.2.1 Blinding

We use catalogue-level blinding to guard ourselves against experimenter bias which may drive our analysis towards known values of cosmological parameters from existing experiments. We transform the shape catalogue in the same way as in the DES-Y3 analysis (Gatti et al. 2021). This blinding method involves changing ellipticity values with the transformation:

$$|\eta| \equiv 2\text{arctan}|\boldsymbol{e}|$$
$$\rightarrow f|\eta|$$

where f is an unknown factor between 0.9 and 1.1 (Gatti et al. 2021), which we keep the same for all four tomographic bins. This transformation limits the ellipticity values within unity and re-scales the estimated shear. Note that DES-Y3 analysis uses two-stage blinding; the first stage is at the catalogue level, and the second is at the level of summary statistics. In this work, we only perform catalogue-level blinding.

We performed all of our null and validation tests and an initial round of internal collaboration review of the manuscript with the blinding factor still included. During this stage, we did not plot or compare the data bandpowers with the theoretical $C_\ell^{\kappa_C \gamma_E}$. We plotted the figures showing parameter inference from the blinded data without the axis values. After we finalized the analysis pipeline, we removed the unblinding factor and updated the manuscript accordingly to discuss the results.

4 METHOD

In this work, we infer the cosmological, astrophysical, and observational systematic parameters using the angular cross-power spectrum between the CMB lensing convergence and the tomographic galaxy weak lensing fields. In this section, we discuss the analysis methodology.

4.1 Simulations

We use simulations of CMB convergence κ_C and galaxy shape γ with realistic noise to validate the analysis pipeline and obtain the covariance matrices for $C_\ell^{\gamma_E}$. Weak-lensing convergence and shear are not expected to be exact Gaussian random fields. A lognormal distribution provides a good approximation of weak lensing convergence and shear fields (Hilbert, Hartlap & Schneider 2011). Generating lognormal simulations is computationally cheap compared to *N*-body simulations and/or ray tracing. The feasibility of the lognormal simulations for the covariance matrices of the power spectrum is discussed in Friedrich et al. (2018).

We simulate κ_C and γ signal maps as correlated lognormal random fields with zero mean using the publicly available code package FLASK (Xavier, Abdalla & Joachimi 2016). We generate full sky, correlated signal maps of both convergence and shear at `Nside` = 2048, corresponding to 1.7 arcmin pixel resolution. To generate signal-only map realizations, inputs to FLASK are (1) the theory angular power spectra describing the auto and cross spectra of convergence field ($\kappa_{C/g}$) for the CMB and the source galaxies ($C_\ell^{\kappa_{C/g}\kappa_{C/g}}$), (2) the galaxy source redshift distribution $n(z)$, and (3) the lognormal shift parameter which determines the skewness of the lognormal distribution for a given variance. The auto and cross-power spectra are computed using CCL with the `halofit` matter power spectrum. $n(z)$ is the DES-Y3 source galaxy redshift distribution, which is also used as input to CCL while computing $C_\ell^{\kappa_{C/g}\kappa_{C/g}}$. We use the same lognormal shift parameter values as used in Friedrich

et al. (2021) and Omori et al. (2023). These are 0.00453, 0.00885, 0.01918, and 0.03287 for four DES-Y3 source redshift bins and 2.7 for the CMB. We then apply the ACT-D56 mask to the convergence fields and the DES-Y3 mask to the shear field to obtain signal-only maps over the respective survey footprints. The DES-Y3 mask used at this stage is a binary mask with a pixel value equal to zero if the pixel does not contain any source galaxy and a value of one otherwise.

We use the following procedure to obtain the κ_C and γ maps with noise that has the correlated signal part. In the simulations, a particular realization of the reconstructed κ_C is generally obtained by reconstructing the lensing convergence from a simulated CMB map that has been lensed by a given κ_C signal realization. However, in this work, we do not perform such an end-to-end κ_C reconstruction with our lognormal signal-only κ_C maps. Instead, we use existing ACT-DR4 κ_C signal realizations and reconstruction simulations. The signal in these simulations is not correlated with our LSS simulations, so they cannot be used directly. Instead, we subtract the signal realization from these reconstructed κ_C maps to obtain a realization of κ_C reconstruction noise. We then add these resultant noise maps to our lognormal κ_C signal-only map generated using FLASK. For these FLASK simulations, we have also generated κ_C signal maps which are correctly correlated with the γ signal. We generate simulations of the noise in the shear (the uncertainty caused by the intrinsic galaxy shape) using the random rotation of galaxy ellipticities in the DES-Y3 shear catalogue: $(e_1+ie_2) \rightarrow \exp(2i\phi)(e_1+ie_2)$, where ϕ is a uniform random number in the range $[0, 2\pi)$. A shear noise map is obtained using this catalogue where the galaxy shapes are rotated. We add these shear noise maps to the shear signal-only maps to obtain shear maps with realistic noise.

4.2 Shear map making

We perform our analysis in harmonic space on the maps prepared in the HEALPIX pixelization. Along with the shape measurements, the DES-Y3 shape catalogue contains weights and METACALIBRA-TION response (R_1, R_2) for each galaxy. The R_1 and R_2 are the diagonals of the response matrix $\mathbf{R}$ discussed in Section 2. While estimating shear from the shape measurement, we do not use the response for each galaxy, but the average response as used in Gatti et al. (2021). We first subtract the non-zero mean of each ellipticity component for each galaxy using the weighted average and then correct for the response using the following expression:

$$\hat{e}_i = \frac{1}{\bar{R}} \left(e_i - \frac{\sum_j w_j e_j}{\sum_j w_j} \right), \tag{9}$$

where the average response $\bar{R}$ for each ellipticity component of four tomographic bins is given in Table 1 and the labels i and j run over all of the galaxies in a given tomographic bin. The above subtraction is carried out for each tomographic bin separately. The shear map for a given bin is obtained from these mean subtracted and response-corrected galaxy shapes. The shear estimate for a given pixel p is the inverse variance weighted average of galaxy ellipticities

$$\gamma(n_p) = \frac{\sum_{i \in p} w_i \hat{e}_i}{\sum_{i \in p} w_i}, \tag{10}$$

where the summation is over all the galaxies that fall within the area of pixel p.

To obtain the mask to be used with the shear maps, we use the sum-of-weights scheme, where we form the map from the inverse variance weights (w_i) given in the DES-Y3 catalogue (Nicola et al.
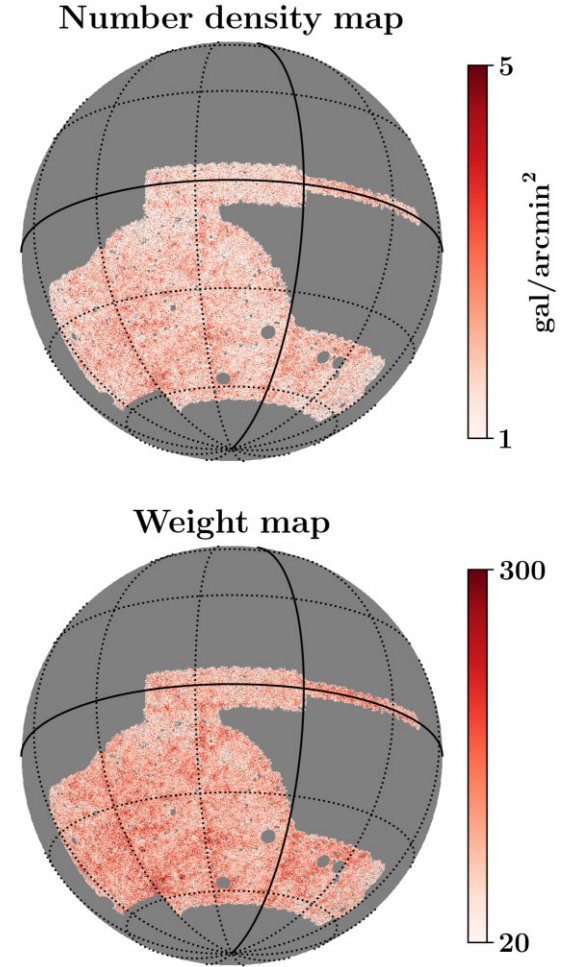

Figure 4. The source galaxy number density map in gal/arcmin^2 unit (top) and the weight map (bottom) for the galaxies in DES-Y3 Bin-4. For the weight map, the value in each pixel is the summation of the inverse variance weights of all the galaxies that fall within that pixel. The weight map is used as the shear field mask without apodization.

2021),

$$W(n_p) = \sum_{i \in p} w_i. \tag{11}$$

We show the representative shear mask in Fig. 4, along with the source galaxy number density map. These maps indicate the inhomogeneity in the galaxy count and their weights. Fig. 5 show the maps of the shear component obtained using the procedure discussed in this section.

4.3 Power spectrum bandpowers and covariance matrix

While computing the angular power spectrum with the partial sky map, one needs to consider the correlations between the spherical harmonic coefficients induced by the mask. This problem is addressed by the pseudo-C_ℓ formalism, such as in the MASTER algorithm (Hivon et al. 2002). The algorithm deconvolves the effect of the mask and provides an estimate of the power spectrum ($\hat{C}_q$) binned over a certain range of multipoles $\ell \in q$. The ensemble average of $\hat{C}_q$ is equal to the weighted average of the underlying angular power spectrum of the full-sky map over a range of multipoles. The bandpower window function specifies the range of multipoles and the multipole weights.
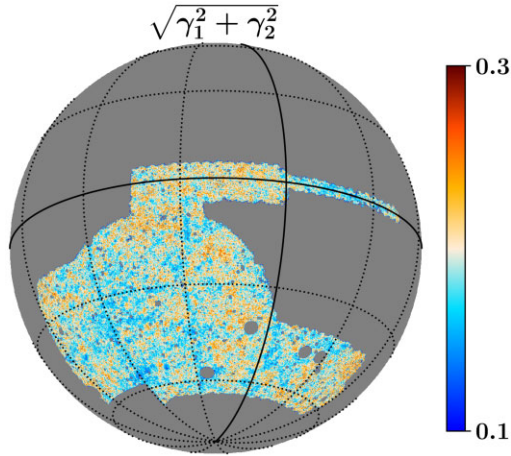
$$\sqrt{\gamma_1^2 + \gamma_2^2}$$

Figure 5. Map of the magnitude of shear ($\sqrt{\gamma_1^2 + \gamma_2^2}$) for the tomographic Bin-4, where the value of shear in each pixel is estimated using equation 10. The map is smoothed with a Gaussian kernel of 12 arcmin FWHM for visual purposes.

To compute these power spectrum bandpowers on the partial sky maps, we use the MASTER algorithm and its application for spin-2 fields (Hikage et al. 2011), as implemented in NAMASTER (Alonso et al. 2019). Given the maps of the two shear components obtained using equation 10 and the map of the CMB lensing convergence, κ_C, we use NAMASTER to estimate the angular power spectrum between κ_C and the spin-2 shear field maps. In harmonic space, the spin-2 field is represented using E and B modes as given in equation 2, and we denote their angular cross-power spectrum with κ_C by $C_\ell^{\kappa_C \gamma_E}$ and $C_\ell^{\kappa_C \gamma_B}$, respectively. We point readers to section 2 of Alonso et al. (2019) for the details of power spectrum estimation in the presence of a sky mask using the pseudo-C_ℓ method.

In NAMASTER, we specify separate masks for the κ_C and γ fields. For κ_C, we use the ACT-DR4 analysis mask for the D56 region. We convert this mask from CAR pixelization to HEALPIX pixelization at Nside = 2048 resolution using the reproject module of the pixell package. The original mask in CAR projection is apodized. We do not introduce any extra apodization in the mask after reprojecting to HEALPIX. This analysis mask is applied to CMB maps used in the quadratic estimator while reconstructing κ_C; hence, the reconstructed κ_C map has the mask implicit in it. We use the square of the analysis mask as the mask implicit in reconstructed κ_C.[4] For the shear field, we use the sum of inverse variance weights mask as expressed in equation 11 and depicted in Fig. 4. This procedure is equivalent to dividing by the variance of the shear estimate in equation 10. Compared to the κ_C mask, the shear mask is highly non-uniform, as evident from Fig. 4. We do not apodize this mask because apodization would lead to losing a substantial sky fraction. Using the simulations described above, we verify that our masking choices do not affect the recovered data vector. In the remaining section, we discuss the computation of pseudo-C_ℓ and validation of the simulations at the power spectrum level.

In the reconstructed κ_C map, lower multipoles are affected by the mean-field bias caused by statistical anisotropy due to non-lensing effects, such as the analysis mask, inhomogeneous noise and other non-idealities in the data. For ACT D56 κ_C, multipoles below $\ell \approx$

[4]This information is specified in NAMASTER using masked_on_input = True keyword argument.

50 are affected by the mean field (Darwish et al. 2021). Hence, we neglect the first bandpower of $C_\ell^{\kappa_C \gamma_E}$ computed in the range $\ell = 0 - 100$. This analysis uses the $C_\ell^{\kappa_C \gamma_E}$ computed at multipoles above $\ell_{min} = 100$. The distribution of matter by the baryonic processes also affects the weak lensing angular power spectrum at small scales. To accurately model these scales, one needs to consider the effect of baryons in the modelling. In this work, we do not consider the modelling of the baryons and choose $\ell_{max} = 1900$ so that the effect of baryons on $C_\ell^{\kappa_C \gamma_E}$ is negligible at the given statistical uncertainty. To assess the effect of baryons, we use the halo model with baryon modelling considered in HMCODE (Mead et al. 2015) as implemented in CAMB (Lewis, Challinor & Lasenby 2000; Howlett et al. 2012). Modelling of baryons in HMCODE is done through two parameters: halo concentration parameter A_{HM} (HMCode_A_baryon) and the halo profile parameter η (HMCode_eta_baryon). We compute theory $C_\ell^{\kappa_C \gamma_E}$ for the fiducial cosmological parameters and over the range of values of A_{HM} and η. For A_{HM}, we consider the range $A_{HM} = 2$ to 4.5 and η is determined by the empirical relation $\eta = 1.03 - 0.11 A_{HM}$ (Mead et al. 2015). We compare theory $C_\ell^{\kappa_C \gamma_E}$ with the uncertainty on $C_\ell^{\kappa_C \gamma_E}$ with ACT-DR4 and DES-Y3. We find that, over the range of baryon parameters considered here, the relative effect of baryons on $C_\ell^{\kappa_C \gamma_E}$ for $\ell > 1000$ can be up to 20 per cent. At the redshift where $W_\kappa^{CMB}(z) W_\gamma^g(z)$ has the peak, $\ell_{max} = 1900$ corresponds to the co-moving wavenumber of $k_{max} \equiv \ell_{max}/\chi(z) = 0.96, 0.72, 0.53, 0.44$ Mpc^{-1} for four DES-Y3 tomographic redshift bins, respectively. The matter perturbations at these scales are non-linear and sensitive to baryonic processes (Mead et al. 2015). However, the effect of baryons is still well within two per cent of the statistical uncertainty on $C_\ell^{\kappa_C \gamma_E}$ up to $\ell = 1900$. Moreover, for the given noise level, the expected SNR of $C_\ell^{\kappa_C \gamma_E}$ is saturated beyond $\ell \approx 1900$. Hence, we choose $\ell = 1900$ as the optimal choice for ℓ_{max} in this analysis. We choose the multipole bin width $\Delta\ell = 300$ with uniform weights for the power spectrum binning.

We compare the pseudo-C_ℓ computed from simulated maps with the input theory power spectrum. In the left column of Fig. 6, we compare the FLASK signal-only simulation bandpowers computed over the survey footprint and the input theory $C_\ell^{\kappa_C \gamma_E}$. We compare the mean of the pseudo-C_ℓ from 511 simulations with the binned input theory power spectrum. We perform the binning of the theory $C_\ell^{\kappa_C \gamma_E}$ while properly taking into account the effect of bandpower window as discussed in section 2.1.3 of Alonso et al. (2019). As shown in the left panel of Fig. 6, we see no significant bias between pseudo-C_ℓ computed from simulated maps and the input $C_\ell^{\kappa_C \gamma_E}$ and conclude that our simulated signal maps are consistent with the appropriate cosmological signal. This also verifies that the mode decoupling by NAMASTER for the given masks gives an unbiased power spectrum estimate. We then compute the pseudo-C_ℓ of the 511 simulations with signal and noise. In the right column of Fig. 6, we compare the mean of these 511 bandpowers with the input theory. Here also, we do not see a significant bias and find that the bandpowers computed from the noisy simulations are consistent with the input theory. This validates the power spectrum computation part of the analysis pipeline.

We use these 511 simulation bandpowers to obtain the covariance matrix for the $C_\ell^{\kappa_C \gamma_E}$ data vector. We expect this covariance matrix to accurately capture features of real data relevant to the power spectrum analysis. These include the non-Gaussianity of the signal modelled as the lognormal field, the inhomogeneous and non-Gaussian nature of κ_C reconstruction noise, the inhomogeneous nature of shear noise arising from variations in the number count and the inverse variance weights. Each simulation bandpower realization is obtained using
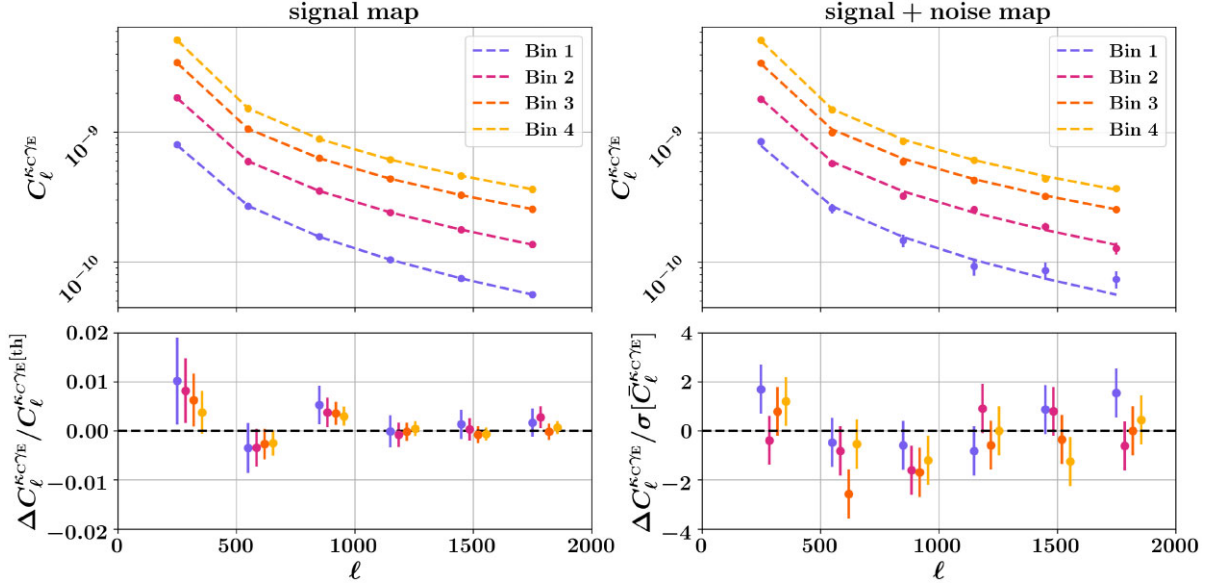
Figure 6. Comparison of mean of $C_\ell^{\kappa_C \gamma_E}$ ($\bar{C}_\ell^{\kappa_C \gamma_E}$) from signal only (left panel) and signal+noise (right panel) simulations with the theory $C_\ell^{\kappa_C \gamma_E}$, enabling us to compare our pipeline against expectations. Left top panel: Comparison between input theory power spectra (dashed line) and the mean of the power spectrum of 511 signal-only simulated maps (points). Left bottom panel: The relative difference between the two. The error bars represent the uncertainty on the mean of 511 simulations. Right top panel: Comparison between input theory power spectra and the mean of the power spectrum of 511 simulated maps with signal and noise. Right bottom panel: The difference between the two in units of the uncertainty on the mean of $C_\ell^{\kappa_C \gamma_E}$. The error bars are the standard deviation of the mean, i.e. $\sigma[\bar{C}_\ell^{\kappa_C \gamma_E}] = \sigma[C_\ell^{\kappa_C \gamma_E}]/\sqrt{N_{\mathrm{sims}}}$.

NAMASTER with the same mask treatment as applied to the data and hence captures the effect of using the partial sky.

We also construct a theoretical covariance matrix for the pseudo-C_ℓ using NAMASTER. This covariance matrix takes into account the effect of the mask, the Gaussian contribution based on the auto and cross theory C_ℓ of κ_C and γ_E, and the noise power spectrum N_ℓ of the respective field. For the κ_C noise power spectrum, we use the mean of the noise power spectra obtained from 511 maps of the κ_C noise simulation. We obtain the shear noise power spectrum, $N_\ell^{\gamma\gamma}$, using the following analytical expression (Nicola et al. 2021):

$$N_\ell^{\gamma\gamma} = A \frac{\sum_i w_i^2 \sigma_{e,i}^2}{(\sum_i w_i)^2}, \tag{12}$$

where A is the sky area and $\sigma_{e,i}^2 = (e_{i,1}^2 + e_{i,2}^2)/2$. The summation in the above equation is carried out only for the galaxies within the common region between DES-Y3 and ACT D56 region. We find that using $N_\ell^{\gamma\gamma} = \sigma_e^2/n_{\mathrm{eff}}$, with the σ_e^2 and n_{eff} values given in Table 1, leads to relatively lower $N_\ell^{\gamma\gamma}$ than the one obtained using equation (12) evaluated for galaxies only over the ACT D56 region. This is because σ_e^2 and n_{eff} given in Table 1 are obtained from all the galaxies within the respective tomographic redshift bin. In contrast, for cross-correlation, we only need σ_e^2 and n_{eff} for the region that overlaps with the ACT D56 region. In Fig. 7, we compare the diagonal of two covariance matrices. We find good agreement between the two covariance matrix estimates. In Fig. 8, we show the correlation matrix obtained from the simulation covariance matrix as well as the Gaussian covariance matrix. With the choice of $\Delta\ell = 300$, we see no significant correlation between nearby bandpowers. Some of the matter lensing the source galaxies in two different redshift bins is the same. This leads to a correlation between the $C_\ell^{\kappa_C \gamma_E}$ corresponding to these redshift bins. The Gaussian covariance part in Fig. 8 clearly shows the non-zero off-diagonal terms that arise due to these correlations, and as expected, the correlations between the
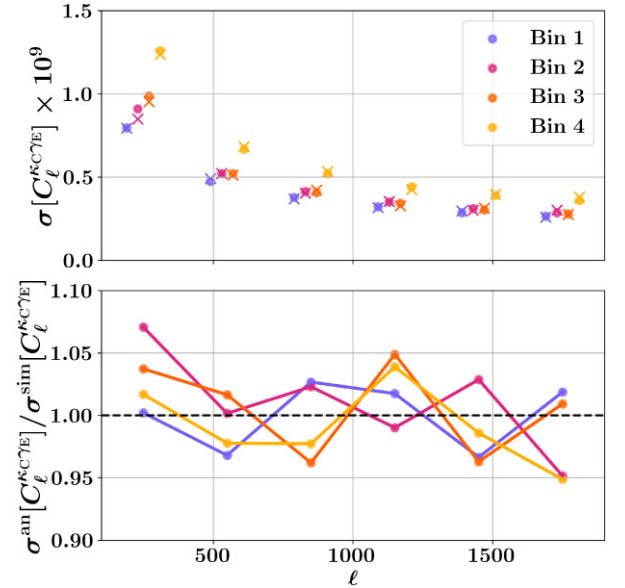

Figure 7. Top: Square root of the diagonal of the analytical (dot) and simulation (cross) covariance matrices for four tomographic bins. Bottom: The ratio of the diagonal of two covariance matrices, indicating agreement between the two within ± 5 per cent.

two highest redshift bins, Bin 3 and Bin 4, are relatively larger. We include this inter-redshift bin correlation in our simulations, which is considered in the parameter inference.

5 LIKELIHOOD AND INFERENCE

To evaluate the likelihood for the $C_\ell^{\kappa_C \gamma_E}$ bandpowers, we make use of the Simons Observatory Likelihoods and Theories (SOLikeT)
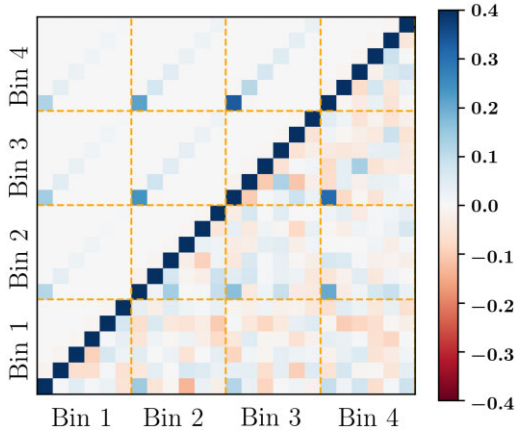
Figure 8. Correlation matrix obtained from the covariance matrix over the multipole range of $\ell = 100$ to 1900 with $\Delta\ell = 300$. The upper triangle shows the elements of the correlation matrix obtained from the analytical covariance matrix, and the lower triangle shows that from the simulation covariance matrix. Note that the colour scale is saturated at ± 0.4 to clearly show the fluctuations in the off-diagonal terms.

framework.[5] SOLikeT is a unified framework for analysing cosmological data from CMB and LSS experiments being developed for the Simons Observatory (SO, Ade et al. 2019). Here we use the KappaGammaLikelihood module to compute the theory $C_\ell^{\kappa_C \gamma_E}$ bandpowers at a given set of parameters $\boldsymbol{\theta}$. This computation uses CAMB (Lewis, Challinor & Lasenby 2000; Howlett et al. 2012) matter power spectra with Limber integrals evaluated by CCL (Chisari et al. 2019). The KappaGammaLikelihood module has been verified to reproduce published results.[6]

5.1 Cosmological model and parameters

We consider a cosmology with fiducial parameters as given by the Planck Collaboration (2020) *Planck* 'base-ΛCDM' TT,TE,EE+lowE+lensing model, with values as described in Table 2. Parameters are held at these fixed values for simulations, while parameter inference runs are initialized centred around these values, then sampled within the prior ranges shown and marginalized over to give results on other parameters. Where no prior is shown, the values are kept fixed throughout. Our main results are the posterior of the parameters Ω_m, σ_8, and $S_8 \equiv \sigma_8 (\Omega_m/0.3)^{0.5}$, where S_8 is the standard parameter optimally constrained by galaxy lensing, in contrast to $S_8^{\rm CMBL} \equiv \sigma_8 (\Omega_m/0.3)^{0.25}$ which is optimally constrained by CMB lensing alone. The left-most panel of Fig. 9 shows a simulation of our data vector (as described in Section 4.1) plotted against predictions from cosmologies with different relevant S_8 values, giving an idea of the constraining power of the data.

5.2 Nuisance model and parameters

Systematic uncertainties on galaxy cosmic shear power spectra are frequently dealt with by marginalizing over simple parametrized models. Here, we consider models of three cases, following the choices in the baseline DES-Y3 analyses:

[5]https://github.com/simonsobs/SOLikeT/
[6]https://github.com/simonsobs/SOLikeT/pull/58#issuecomment-1213989444 where the measurement of Hand et al. (2015) is reproduced.

Table 2. The parameters and priors used in the model specification within a ΛCDM cosmology. Fiducial values are used for simulations and initialization of inference chains. Priors are either uniform $\mathcal{U}[\min, \max]$ or Gaussian $\mathcal{N}(\mu, \sigma)$. Unlisted other cosmological parameters and model choices are fixed to their default values in CAMB v1.3.5 (Lewis et al. 2022).

Parameter	Fiducial	Prior
Cosmology sampled		
$\Omega_c h^2$	0.120	$\mathcal{U}[0.05, 0.99]$
$\log(A_s 10^{10})$	3.042	$\mathcal{U}[1.6, 4.0]$
H_0	67.36	$\mathcal{U}[40, 100]$
Cosmology fixed		
$\Omega_b h^2$	0.0224	–
n_s	0.9649	–
$\sum m_\nu$ [eV]	0.06	–
Galaxy IA		
$A_{\rm IA}$	0.35	$\mathcal{N}(0.35, 0.65)$
$\eta_{\rm IA}$	1.66	$\mathcal{N}(1.66, 4)$
Galaxy redshift calibration		
Δz_1	0.0	$\mathcal{N}(0.0, 0.018)$
Δz_2	0.0	$\mathcal{N}(0.0, 0.015)$
Δz_3	0.0	$\mathcal{N}(0.0, 0.011)$
Δz_4	0.0	$\mathcal{N}(0.0, 0.017)$
Galaxy shear calibration		
m_1	-0.006	$\mathcal{N}(-0.006, 0.009)$
m_2	-0.020	$\mathcal{N}(-0.020, 0.008)$
m_3	-0.024	$\mathcal{N}(-0.024, 0.008)$
m_4	-0.037	$\mathcal{N}(-0.037, 0.008)$

(i) Multiplicative shear bias: The process of measuring weak lensing shear from noisy images can induce biases on the inferred power spectrum (see, e.g. MacCrann et al. 2022). For current experiments, including DES-Y3, it has been shown to be adequate to model these using a single multiplicative parameter per tomographic bin m_i (Heymans et al. 2006; Huterer et al. 2006; Kitching, Deshpande & Taylor 2020), which modifies the power spectra as

$$C_\ell^{\kappa_C \gamma_E, i} \rightarrow (1 + m_i) C_\ell^{\kappa_C \gamma_E, i}. \tag{13}$$

In the second from the left panel of Fig. 9 we show the effect of varying the m nuisance parameter on the $C_\ell^{\kappa_C \gamma_E}$ spectra alongside our simulated measurements for tomographic bin 4.

(ii) Source redshift distribution calibration: Galaxy shear power spectra are highly sensitive to the redshift distribution function $n(z)$ within each tomographic bin of the sources used. Where the samples are selected using photometric information, as is the case in DES-Y3, the estimated $n(z)$ may have significant uncertainties in both the overall mean redshift and detailed shape. Though more sophisticated parametrizations of these uncertainties exist and are expected to be important for near-future experiments, it has been shown that for the weak lensing source galaxies in DES-Y3, it is adequate only to consider the uncertainty on the mean of the $n(z)$ within each tomographic bin (e.g. Cordero et al. 2022). We include four additional nuisance parameters Δz_i for a shift in the mean of each tomographic bin: at each likelihood evaluation step, we shift the distribution in each tomographic bin i according to:

$$n_i(z) \rightarrow n_i(z + \Delta z_i). \tag{14}$$

The second from the right panel of Fig. 9 shows the effect of varying the z nuisance parameter on the $C_\ell^{\kappa_C \gamma_E}$ spectra alongside our simulated measurements for tomographic bin 4.

(iii) Galaxy IAs: The use of galaxy images as a proxy for gravitational shear relies on the assumption that intrinsic galaxy
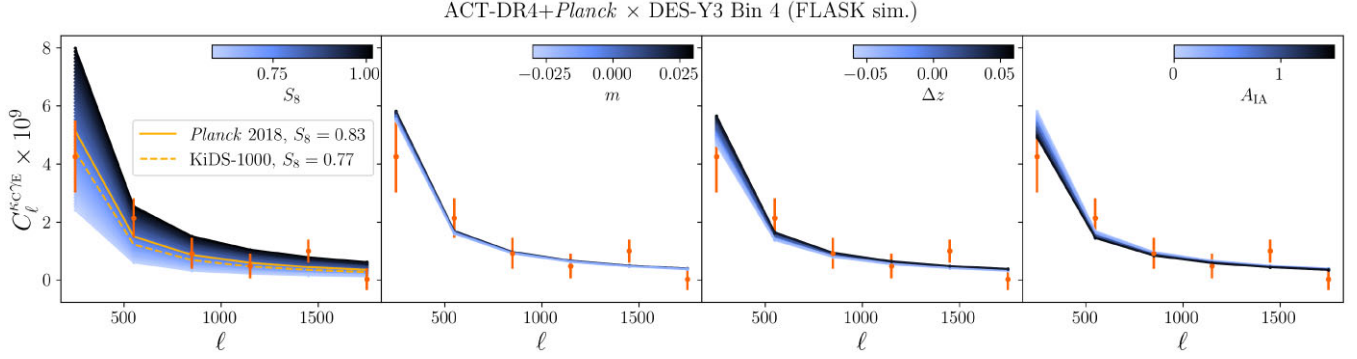
Figure 9. Illustrative changes in predicted data vectors as the cosmological and nuisance parameters are individually varied, compared to the simulated data vector described in Section 4.1 (to be concise, we only show tomographic Bin 4 as this is the highest SNR bin). The left-most panel also shows cosmologies with S_8 as found by *Planck* 2018 primary CMB (Planck Collaboration 2020) and the KiDS-1000+BOSS+2dFLenS galaxy clustering and weak lensing survey (Heymans et al. 2021) as examples of the range of values present in the current literature.

shapes are randomly oriented, which is not the case in reality. Physically close pairs of galaxies will tend to align their major axes towards overdensities local to them in positively correlated 'intrinsic–intrinsic' (II) alignments. Negative 'shear–intrinsic' (GI) correlations are also created when distant galaxies are tangentially sheared by lensing from foreground overdensities, which more nearby galaxies are gravitationally aligned towards. The power spectrum of the contaminating IAs can be physically modelled in a number of ways (see Samuroff et al. 2023, and references therein). Here, we adopt the Non-linear Linear Alignment (NLA) model (Bridle & King 2007; Hirata et al. 2007) which makes the simplifying assumption that IAs are from E-mode GI alignments only, neglecting the intrinsic–intrinsic B-mode term which is also possible to consider in the $C_\ell^{\kappa_{CMB}\gamma_E}$ observable. The NLA model treats the GI alignment power spectrum as a simple scaling of the matter power spectrum with a redshift evolution. We infer the two parameters A_{IA} and η_{IA} across all tomographic bins, corresponding to a substitution in the galaxy lensing kernel:

$$W_\gamma^g(z) \rightarrow W_\gamma^g(z) - A_{IA} C_1 \rho_{cr} \frac{\Omega_m}{G(z)} n(z) \left(\frac{1+z}{1+z_0} \right)^{\eta_{IA}}. \quad (15)$$

Here, z_0 is pivot redshift fixed to 0.62 as in Secco et al. (2022), $G(z)$ is the linear growth factor and $C_1 = 5 \times 10^{14} M_\odot^{-1} h^{-2} \text{Mpc}^3$ is the normalization constant. The rightmost panel of Fig. 9 shows the effect of varying A_{IA} on the theory spectra for tomographic bin 4. Whilst the more sophisticated Tidal Alignment and Tidal Torquing (TATT) model was adopted as fiducial for the DES-Y3 3×2pt analysis of Abbott et al. (2022), when considering only the shear part of the data, Secco et al. (2022) find a mild preference for the simpler NLA model (row three of Table III in that work) which we therefore choose to adopt for reasons of both model and implementation simplicity.

5.3 Likelihood computation

We compute a simple Gaussian likelihood ($\mathcal{L}$) between our data vector bandpowers and binned theory vector at a given set of cosmological and nuisance parameters $\boldsymbol{\theta}$ using the covariance matrix, $\mathbb{C}$, calculated in Section 4.3:

$$-2 \ln \mathcal{L} = \sum_{\ell\ell'} \left[\hat{C}_\ell^{\kappa_{CMB}\gamma_E} - C_\ell^{\kappa_{CMB}\gamma_E}(\boldsymbol{\theta}) \right] \mathbb{C}_{\ell\ell'}^{-1} \left[\hat{C}_{\ell'}^{\kappa_{CMB}\gamma_E} - C_{\ell'}^{\kappa_{CMB}\gamma_E}(\boldsymbol{\theta}) \right], \quad (16)$$

where $\hat{C}_\ell^{\kappa_{CMB}\gamma_E}$ is the data vector and $C_\ell^{\kappa_{CMB}\gamma_E}$ is the model power spectrum. The posterior probability for the parameters is then propor-

tional to the likelihood multiplied by the priors (Π): $P(\boldsymbol{\theta}|\hat{C}_\ell^{\kappa_{CMB}\gamma_E}) \propto \mathcal{L}(\hat{C}_\ell^{\kappa_{CMB}\gamma_E}|\boldsymbol{\theta})\Pi(\boldsymbol{\theta})$. The choices of prior distributions are detailed in Section 5.4.

5.3.1 Hartlap correction

Because the fiducial covariance matrix is estimated from a finite number of simulations, the inverse covariance matrix used in the likelihood computation is known to be a biased estimate of the true inverse covariance matrix (Anderson 2003; Hartlap, Simon & Schneider 2007). To account for this, we apply the well-known Hartlap correction to the inverse covariance matrix:

$$\mathbb{C}^{-1} \rightarrow \alpha \mathbb{C}^{-1}; \alpha \equiv \frac{N_{sims} - N_{data} - 2}{N_{sims} - 1}, \quad (17)$$

where N_{sims} is the number of simulations and N_{data} is the length of the data vector. We use the corrected covariance matrix for computing our likelihood. For our 511 simulations and 24 data points, the size of the Hartlap correction is $\alpha = 0.951$. The choice of $\Delta\ell = 300$ reduces the total number of data points in the data vector, which is optimal compared to $\Delta\ell < 300$ because, for a given number of simulations, fewer data points minimize the impact of the Hartlap correction.

5.4 Prior choice

In Table 2, we show the set of cosmological and nuisance parameters varied in our Monte Carlo chains. Fiducial cosmological parameters (the values at which simulations are performed and that in inference sampling runs are used to initialize the chains) are chosen to coincide with those of the *Planck* Collaboration's 'base-ΛCDM' `TT,TE,EE+lowE+lensing` model from Planck Collaboration (2020) and priors are wide enough to capture all reasonable cosmologies at the time of writing. Whilst our $C_\ell^{\kappa_{CMB}\gamma_E}$ observable depends only weakly on the Hubble expansion parameter H_0, we found in initial runs based on a simulated data vector that when this parameter was kept fixed, a sharp boundary appeared in the two-dimensional (σ_8, Ω_m) plane, with the lower right section of the 'banana' shape being cut off. This did not affect the posterior on S_8 but did lead to an artificial bi-modality in the one dimensional Ω_m constraint. Allowing H_0 to vary removed this effect and is in line with the prior treatments of CMB lensing and cross-correlation data vectors (e.g. Chang et al. 2023; Madhavacheril et al. 2023).

5.5 Posterior sampling

We sample from the posterior using the Markov Chain Monte Carlo Metropolis sampler distributed with Cobaya (Lewis & Bridle 2002; Lewis 2013; Torrado & Lewis 2019, 2021). We first run a chain in our fiducial parametrization and with the simulated data vector to convergence without defined scales for the mixed Gaussian-exponential proposal distribution used for taking steps[7] We subsequently use the proposal covariance matrix learned during this chain to speed up convergence for all subsequent chains. We regard chains as converged when the Gelman-Rubin criteria reach a value $R - 1 < 0.01$ and the first 30 per cent of chains are removed as burn-in. For all of our chains, this results in a number of effective samples in the range of 1500–2000.

6 VALIDATION OF DATA AND METHOD

We validate the data vector using two null tests and check for systematic contamination from Galactic dust and stars. Before applying it to the data, we validated the parameter inference methodology using simulations. This includes checking for the absence of bias in the inferred parameters, robustness to the choice of the covariance matrix, and robustness to the effect of the intrinsic galaxy alignment modelling.

6.1 Data vector null tests

We check the data for some non-idealities that may be present. We compute the χ^2 of the statistic under consideration, for which we set PTE = 0.05 as a threshold for considering the test failed. Our unblinding decision was based on the χ^2 and PTEs computed with bandpowers of four redshift bins considered together. We consider a null test to be passed if the PTE exceeds this threshold.[8]

At linear order and under the Born approximation, weak lensing of galaxies by LSS is not expected to give rise to B-modes in the shear map. Therefore, we do not expect any significant B-mode signal of cosmological origin in the shear map. Moreover, obtaining E and B modes from the partial sky shear maps can cause mixing between E and B modes. In the absence of such spurious B-modes, the correlation of the B-modes in the shear maps with the κ_C is expected to be consistent with zero. In Fig. 10, we show the $C_\ell^{\kappa_C \gamma_B}$ bandpowers for four redshift bins with their error bars. With the blinded data vector, we find the four data vectors together are consistent with zero with PTE = 0.81, indicating the absence of spurious B-modes in the shear data. The PTEs for the individual redshift bin bandpowers are 0.47, 0.75, 0.57, and 0.59, respectively.

We also correlate the κ_C map with the shear map obtained from the DES-Y3 catalogue, where ellipticities are randomly rotated. The random rotation is expected to wash out any cosmological signal in the shear maps and, indeed, is how we obtain the shear noise for the mock shear simulations, as discussed in Section 4.1. Hence, the correlation of these maps with the κ_C map tests for any non-cosmological features in shear maps that may correlate with the κ_C map. From Fig. 10, with the blinded data vector, we find this correlation is also consistent with zero with PTE = 0.19. The PTE
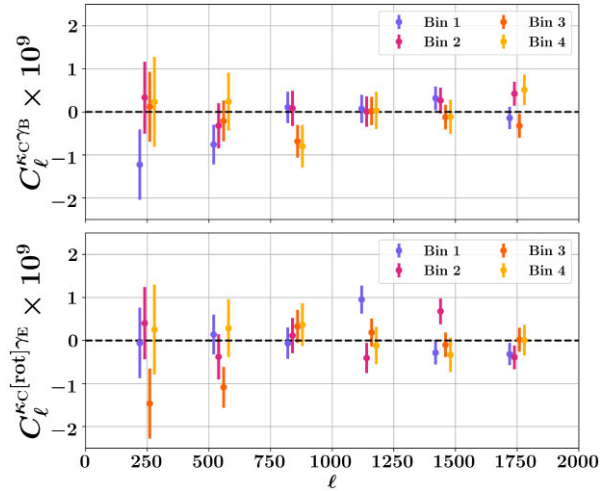
Figure 10. Top: The power spectrum between κ_C and the B-mode of the shear ($C_\ell^{\kappa_C \gamma_B}$). Bottom: The correlation between κ_C and the E-mode of the shear map ($C_\ell^{\kappa_C[\mathrm{rot}]\gamma_E}$) obtained from the catalogue in which DES-Y3 catalogue ellipticities are randomly rotated. The error bar indicates 1σ uncertainty of the statistic. We find both sets of bandpowers to be consistent with zero.

values for individual redshift bin bandpowers are 0.07, 0.20, 0.19, and 0.96. Note that we do not regard the 0.96 as a failure, as these per-bin PTE numbers were not part of our unblinding criteria. For the larger set of PTEs generated by including per-bin calculations, it is more likely that a failure appears by chance from sampling this part of the Uniform distribution expected for the PTE values. These tests provide an important check of the analysis pipeline.

We obtain the covariance matrices for both tests using 511 simulations. For the B-mode null test, the covariance matrix is obtained using $C_\ell^{\kappa_C \gamma_B}$ bandpowers computed using 511 simulations. For the rotation null test, we compute $C_\ell^{\kappa_C \gamma_E}$ bandpowers; hence the covariance matrix is the same as used for the signal $C_\ell^{\kappa_C \gamma_E}$ bandpower.

6.2 Diagnostic tests using survey property maps

Any systematic effect or contamination (S) that simultaneously affects both the observables, κ_C reconstructed from the observed CMB and γ estimated using galaxy shape measurements, can lead to a bias in the measurement of $C_\ell^{\kappa_C \gamma_E}$. For example, the Galactic dust can affect CMB lensing reconstruction through its presence in the CMB map, and the extinction by dust can affect the measurement of galaxy properties. The following statistic captures the amplitude of contamination to $C_\ell^{\kappa_C \gamma_E}$ coming from a given survey property S (Omori et al. 2019; Chang et al. 2023):

$$X_\ell^S = \frac{C_\ell^{\kappa_C S} C_\ell^{\gamma_E S}}{C_\ell^{SS}}. \tag{18}$$

In this work, we consider two survey properties: dust extinction, where S is the map of E(B-V) reddening (Schlegel, Finkbeiner & Davis 1998) and stellar density, where S is the map of stellar density (Abbott et al. 2021; Sevilla-Noarbe et al. 2021; Sánchez et al. 2023). In Fig. 11, we show X_ℓ^S for both survey properties with its error bar. We obtained the error bar using the delete-one patch jackknife method, where we used 28 jackknife samples of the data and survey property maps. For both survey properties, the effect on $C_\ell^{\kappa_C \gamma_E}$ is within a few per cent of the error on $C_\ell^{\kappa_C \gamma_E}$ and hence is of less concern. For dust extinction X_ℓ, we obtain the PTE for four bins as 0.895, 0.698, 0.769, and 0.659, indicating no significant detection of

---

[7]As described in https://cobaya.readthedocs.io/en/latest/sampler_mcmc.html#covariance-matrix-of-the-proposal-pdf.

[8]Unblinding of the data vector was performed assuming a one-sided PTE threshold, with PTE < 0.05 indicating a failed null test. However, as demonstrated in this section, the data vectors for the full data set pass the null test even when considering two-sided PTE distributions.
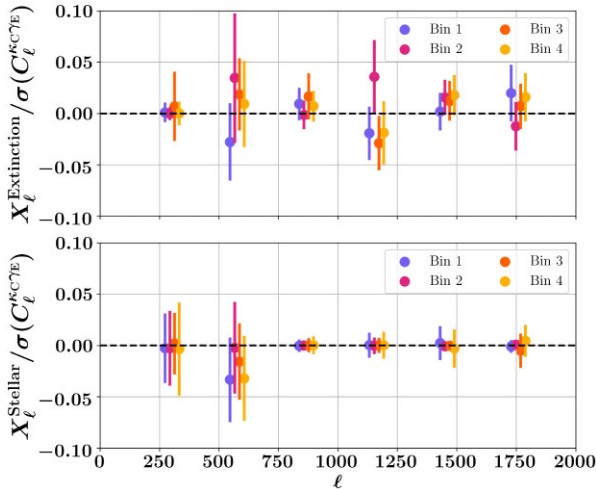
Figure 11. Survey property correlation statistics X_ℓ in units of error bar of $C_\ell^{\kappa C \gamma_E}$, for the dust extinction map (top panel) and the stellar density (bottom panel). The error bars are obtained using X_ℓ computed over 28 jackknife samples of the data. For both survey properties, X_ℓ^S is less than 5 per cent of the error bar on $C_\ell^{\kappa C \gamma_E}$ and consistent with zero.

dust contamination in cross-correlation. For the stellar density, the PTE values are 0.993, 0.999, 0.999, and 0.992. Whilst these PTE values are high and close to one, they indicate an over-consistency with zero according to the estimated error bars. The jackknife method overestimates the error bar in general (Norberg et al. 2009; Favole et al. 2021). Therefor, we do not regard high PTE as problematic in the case of a diagnostic test.

6.3 Model validation

6.3.1 IA model robustness

In order to assess the robustness of our inference to the model chosen for intrinsic galaxy alignments, we create two simulated data vectors, one without any IA signal and one in which the observed angular power spectrum C_ℓs have additional power added from a NLA model as described in equation (15) with the fiducial parameter values $\{A_{\rm IA}, \eta_{\rm IA}\} = \{0.35, 1.66\}$ (corresponding to the mean posterior values from DES-Y3 shear-only analysis in table III of Secco et al. 2022) as shown in Table 2. In Fig. 12, we show the stability of our measurement of S_8 to the choice of IA model, with no significant parameter shifts observed when considering mismatched choices of model and data (e.g. when the NLA model is used on a data vector with no IA signal and vice-versa). We chose to include the full NLA model parametrization for our fiducial inference runs on the data.

Within this parametrization, we choose to include an informative prior on $A_{\rm IA} \sim \mathcal{N}(0.35, 0.65)$ and $\eta_{\rm IA} \sim \mathcal{N}(1.66, 4)$, with prior widths a factor four wider than the posterior on NLA IA parameters found in DES-Y1 data from the 3×2pt analysis of Abbott et al. (2018). Note that the DES-Y1 data are in a sky region not included in our analysis so this prior can be regarded as independent. We refer to this prior as our 'fiducial prior' and it is shown throughout as black unfilled contours. In order to assess the impact of this choice, we also run an inference chain on the simulated data vector with broad priors $\mathcal{U}(-5, 5)$ on both parameters, matching the *priors* used in the DES-Y3 analyses. Note that the latter is a broader prior in the sense that it is less localized in the $A_{\rm IA}$ direction compared to the fiducial prior. The results can be seen in Fig. 13. Here, it
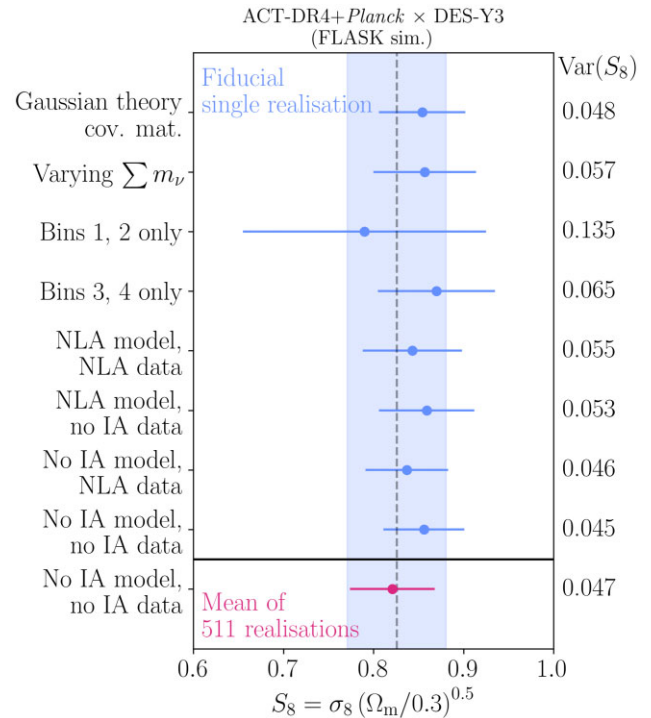
Figure 12. The stability of the recovery of the S_8 parameter from our simulated data vector as we change the model used for the inference. The dashed vertical line represents the true value of the input to the simulation, and the shaded band is the error bar in the fiducial model setup. Note that the slightly (but not significantly) high value recovered in the upper rows is consistent with what is expected for this single realization (see Fig. 14). The final row shows the result for one model using a data vector which is the mean of 511 realizations.
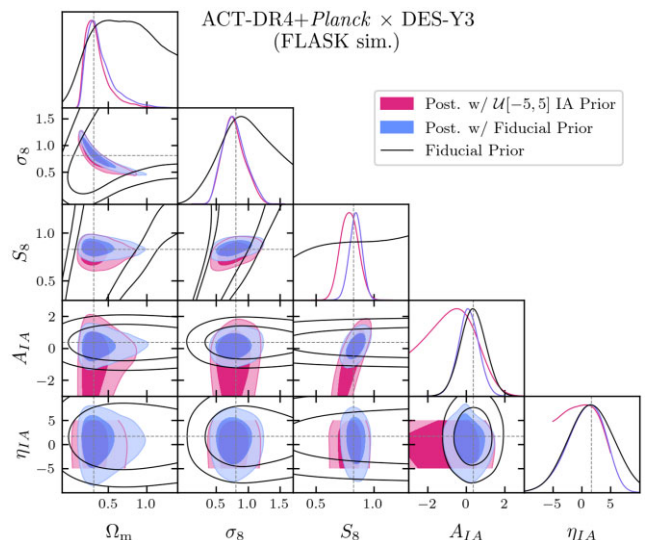
Figure 13. Posteriors showing recovery of the input model from data simulations under the fiducial prior (blue) and an alternate prior choice on galaxy IA parameters (red), that is less localized in $A_{\rm IA}$ direction. The fiducial prior (black) is informed by the DES-Y1 cosmic shear analyses (which use data independent from those used here) and expectations for the NLA model. The wide uninformative prior causes the mild correlation between $A_{\rm IA}$ and S_8 to drag the posterior on the latter to lower values. See text for further discussion.

can be seen that whilst the 1D posteriors on Ω_m and σ_8 are not affected, a mild degeneracy between A_{IA} and S_8 causes a widening of the posterior on S_8 and shift of the peak to lower values. For positive values of A_{IA}, the constraint is relatively unaffected by the choice of prior, and we can indeed see some constraining power of the data appearing due to the similar upper limits from both the wide and the informative prior. For negative values of A_{IA}, it can be seen that the lower limit is dominated by the prior in the fiducial case, with the posterior extending significantly further for the wide prior. This lack of constraining power causes a 'projection effect', which lowers the inferred value of S_8. However, the galaxy formation physics represented by the NLA IA model is expected to result in $A_{IA} > 0$ for red galaxies, and this has been observationally shown to be the case (with KiDS+GAMA Johnston et al. 2019 find $A_{IA}^{Red} = 3.18^{+0.47}_{-0.46}$ and with DES-Y1 Samuroff et al. 2019 find $A_{IA}^{Red} = 2.38^{+0.32}_{-0.31}$). For blue galaxies in the NLA model, $A_{IA} < 0$ is possible, but observations have so far been consistent with zero and inconsistent with large negative values (Johnston et al. 2019 find $A_{IA}^{Blue} = 0.21^{+0.37}_{-0.36}$ and Samuroff et al. 2019 find $A_{IA}^{Blue} = 0.05^{+0.10}_{-0.09}$). For weak lensing samples such as DES-Y3, which contain a mixture of red and blue galaxies, with red fraction $f_{Red} \sim 20$ per cent this means $A_{IA} = A_{IA}^{Red} f_{Red} + A_{IA}^{Blue}(1 - f_{Red})$ is even more constrained to be positive. Motivated by these considerations, we keep the informative prior on IA parameters for the fiducial analysis.

6.3.2 Neutrino model robustness

We chose as our baseline model three neutrinos of degenerate mass, consistent with the model choice of the Abbott et al. (2022), with $\sum m_\nu = 0.06\,\mathrm{eV}$ in our fiducial analysis. We find that differences between our $C_\ell^{\kappa C \gamma E}$ observable are at most ~ 0.5 per cent when comparing three degenerate neutrinos to the normal hierarchy case and at most ~ 2 per cent when comparing to a single-massive neutrino scenario.

The relevant row of Fig. 12 shows the stability of our S_8 measurement to the marginalization over the sum of neutrino mass, with a uniform prior $\sum m_\nu\,[\mathrm{eV}] \sim \mathcal{U}[0.0, 1.0]$, in this model.

6.4 Covariance matrix validation

In addition to the covariance matrix computation with FLASK simulations, as detailed in Section 4.3, we also construct an analytical Gaussian covariance matrix for the pseudo-C_ℓ estimator. The covariance matrix estimated using simulation bandpowers is expected to model non-Gaussian contributions more correctly than the theoretical case but suffers from realization noise effects since it is an average over the finite number of simulations. The results of parameter constraints obtained using the analytical covariance matrix are shown in the relevant row of Fig. 12. As can be seen, both methods give consistent posteriors on our simulated data vector. Therefore, we choose to continue with the simulation-based covariance matrix. This choice is somewhat arbitrary, but on the understanding that as the constraining power of the data improves with future data releases, the effects modelled in the simulations will become more significant.

6.5 Recovery of input model from mock data

In order to verify that our inference pipeline is capable of making an unbiased recovery of cosmological parameters, we run it on a data vector recovered from one of the 511 FLASK simulations described in Section 4.1. The results of this analysis are shown in
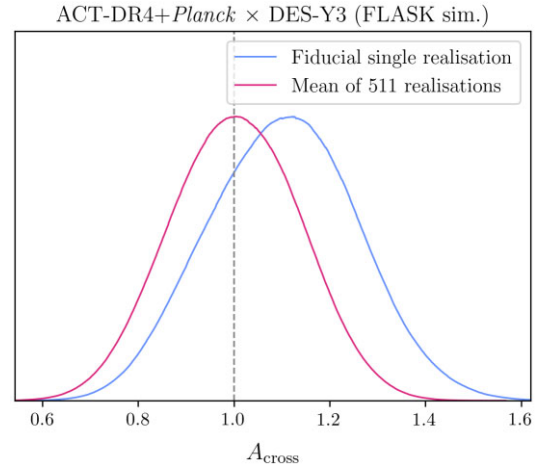
Figure 14. Recovery of the A_{cross} parameter from our simulated data vector. All cosmological and nuisance parameters are held at their true input values, and A_{cross} is an overall amplitude parameter for the $C_\ell^{\kappa C \gamma E}$ spectra, which has the value one at the true input model.

Fig. 13 for cosmological and IA parameters. In Figs B1 and B2, we show the posterior and prior, including those for observational nuisance parameters, but zoomed out to show the full shapes of the prior. The priors are specified in Table 2 and are shown as unfilled contours in the space of the inferred parameters, indicating the level of information gained from the data (or lack of it in the case of the prior-dominated nuisance parameters). As can be seen, all inferred parameters are recovered with biases smaller than the 68 per cent credible interval, as may be expected from realization noise. In addition to this full parameter inference on a single simulation, we have also inferred only the A_{cross} parameter for this simulation *and* a data vector which is the mean of the 511 simulations. A_{cross} is a phenomenological parameter which modifies the overall amplitude of the lensing spectra with respect to that predicted by a model with a fixed set of cosmological parameters (here, the true input parameters to the simulation):

$$C_\ell^{\kappa C \gamma E}{}_{obs} = A_{cross} C_\ell^{\kappa C \gamma E}{}_{true} \tag{19}$$

As shown in Fig. 14, this gives a mean value and 68 per cent credible interval of $A_{cross} = 1.00 \pm 0.13$ for the mean data vector and $A_{cross} = 1.10 \pm 0.15$ for the fiducial realization, confirming the finding that this single realization has a random fluctuation towards higher clustering amplitude S_8, as seen in the full inference in Fig. 12.

6.6 Internal consistency

In order to test the robustness of our result, we perform the inference on a number of different splittings of the full data set. These involve (i) leaving out data from individual tomographic bins in turn and (ii) only using data from an individual tomographic bin in turn. The results of these runs are shown in Fig. 15. These checks were performed before the blinding factor applied to the DES shear catalogue (see Section 3.2.1 for details) was removed in order to act as an extra confirmation of the adequacy of the analysis pipeline. As can be seen, each data split is consistent with all others within the expected scatter, and the behaviour of the error bars matches physical expectations, with progressively larger amounts of cosmic shear lensing signal contained in higher redshift tomographic bins.
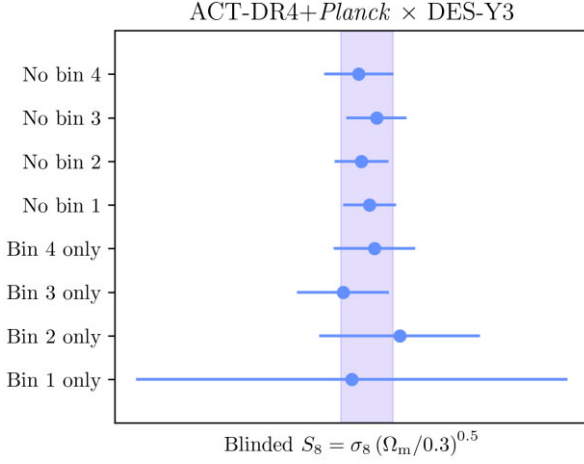
Figure 15. Stability of our 1D marginalized measurement of S_8 when using different parts of the full fiducial data vector, with the fiducial result shown as the shaded band. In each row, we either remove a single DES tomographic bin or use the data from only one.

7 RESULTS

With the above work demonstrating that we have a data vector passing null tests for systematics contamination and that we have a working unbiased measurement pipeline, we now present the results using our fiducial ACT-DR4+*Planck*-tSZ deprojected data vector. We unblind the data vector by obtaining the numerical value of the blinding factor f (as described in Section 3.2.1) and applying the inverse of the blinding transformation to the catalogue shear values. We then re-make our maps and two-point data vectors and proceed. Fig. 16 shows the data for four tomographic bins along with the best fit theory model $C_\ell^{\kappa_C \gamma_E}$. As a validation, we also compute the full set of results for $C_\ell^{\kappa_C \gamma_E}$ with the ACT-DR4-only κ_C, and these are presented in Appendix A.

7.1 Lensing amplitude $A_{\rm cross}$

We first consider the case in which we fix all other parameters to our fiducial values as in Table 2 and vary only the normalization ($A_{\rm cross}$) of the observed $C_\ell^{\kappa_C \gamma_E}$ spectrum relative to the prediction from this model:

$$C_\ell^{\kappa_C \gamma_E}{}_{\rm obs} = A_{\rm cross} C_\ell^{\kappa_C \gamma_E}{}_{\rm Planck} \qquad (20)$$

Under a uniform prior of $A_{\rm cross} \sim \mathcal{U}[0.0, 2.0]$ we find a measurement of $A_{\rm cross} = 0.84^{+0.16}_{-0.13}$ indicating agreement with the *Planck* result but mildly favouring a lower amplitude. This compares to previous determinations of $A_{\rm cross}$ using $C_\ell^{\kappa_C \gamma_E}$ data: from POLARBEAR (polarisation lensing)×HSC of 1.70 ± 0.48 (Namikawa et al. 2019); from *Planck*×HSC of 0.81 ± 0.25 (Marques et al. 2020) and ACT+*Planck*×KiDS-1000 of 0.69 ± 0.14 (Robertson et al. 2021). Other previous measurements of $A_{\rm cross}$ from $C_\ell^{\kappa_C \gamma_E}$ have used earlier *Planck* data releases for the baseline cosmology, so are not directly comparable: from ACT×CS82 (Hand et al. 2015); from *Planck*×CFHTLenS (Liu & Hill 2015); from SPT+*Planck*×DES-Science Verification (Kirk et al. 2016); from *Planck*×RCSLenS and CFHTLenS (Harnois-Déraps et al. 2016); from *Planck*×KiDS-450 (Harnois-Déraps et al. 2017); from *Planck*×SDSS (Singh, Mandelbaum & Brownstein 2017) and from SPT+*Planck*×DES-Y1 (Omori et al. 2019). We have not considered the degeneracy between $A_{\rm cross}$ and $A_{\rm IA}$ parameters, which will be relevant in future

higher SNR measurements. This degeneracy can be broken with the self-calibration of IA, as demonstrated in Yao et al. (2023).

7.2 Matter clustering S_8 and other parameters

In Fig. 17, we show the inferred posterior on cosmological parameters from the fiducial ACT-DR4+*Planck*×DES-Y3 data vector. The ten galaxy weak lensing nuisance parameters (galaxy IA, redshift calibration, and shear calibration) are also varied but are prior-dominated and omitted in the plot, as is the H_0 parameter (see Appendix B for the plot including them). We also show the constraints on the cosmological parameters from other experiments. We chose these experiments as being external data sets using very different techniques to measure the same cosmological parameters: the *Planck* 2018 primary CMB result from Planck Collaboration (2020), and the KiDS-1000 3×2pt result from Heymans et al. (2021). Though of lower constraining power, our result contains fully independent data and probes a different set of redshift and physical scales to the two other experiments (see Fig. 1). Additionally, we show in Fig. 18 our 1D marginalized measurement of the S_8 parameter alone against a further catalogue of other measurements (SPT+*Planck*×DES-Y3 Chang et al. 2023; ACT-DR4+*Planck*×KiDS Robertson et al. 2021; DES-Y3 shear only Amon et al. 2022, Secco et al. 2022; KiDS-100 shear only Asgari et al. 2021; DES-Y3 3×2pt Abbott et al. 2022; KiDS-1000 3×2pt Heymans et al. 2021; *Planck* 2018 Primary CMB Planck Collaboration 2020). Summary statistics from our inference for the full set of parameters are shown in Table 3. The marginalized mean values and 1D 68 per cent credible regions for the matter density parameter and the amplitude of the fluctuations in the matter distribution are

   (i) $\Omega_m = 0.338^{+0.05}_{-0.17}$;
   (ii) $\sigma_8 = 0.79^{+0.16}_{-0.19}$;
   (iii) $S_8 = 0.782 \pm 0.059$.

This inference is drawn when informative priors are used on the nuisance parameters. Constraints on the density of the matter Ω_m, even if not most precise, are still a significant improvement over the assumed prior on Ω_m. The value of S_8 inferred in this analysis is consistent with that inferred from the *Planck* TT,TE,EE+lowE CMB measurements $S_8 = 0.834 \pm 0.016$ (Planck Collaboration 2020) with the difference of 0.85σ, when adding the statistical uncertainties in quadrature to obtain the uncertainty on the difference. It is also consistent with the $S_8 = 0.766^{+0.020}_{-0.014}$ inferred using KiDS-1000 3×2pt analysis (Heymans et al. 2021), with around 0.3σ difference. A companion study performs the cross-correlation analysis of ACT-DR4 D56 κ_C and DES-Y3 MAGLIM galaxies finding $S_8 = 0.75^{+0.04}_{-0.05}$ (Marques et al. 2023), which differs only by 0.4σ with the S_8 inferred in this work.

7.3 S_8 at different redshifts

As discussed in Section 1, across the multiple measurements of S_8 from various observables, it has been noted that higher redshift probes often favour a higher value (e.g. the primary CMB in Aiola et al. 2020; Planck Collaboration 2020; Dutcher et al. 2021), whilst lower redshift ones favour a lower value (e.g. galaxy weak lensing in Heymans et al. 2021; Abbott et al. 2022; Miyatake et al. 2023; More et al. 2023; Sugiyama et al. 2023). In light of this, we split our data vector into two different subsets and constrain the S_8 parameter independently in each one. One subset contains only the spectra made with DES-Y3 tomographic bins 1 and 2 (covering redshifts $0 < z \leq 0.63$ and with the resulting $C_\ell^{\kappa_C \gamma_E}$ kernel peaking below $z = 0.5$), and
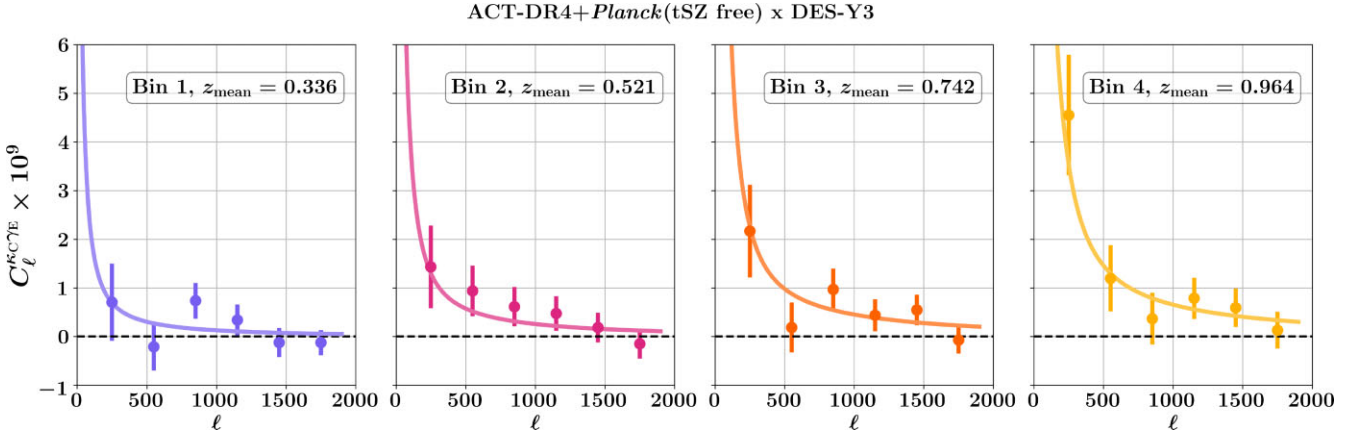
ACT-DR4+*Planck*(tSZ free) x DES-Y3

Figure 16. The points with error bar show $C_\ell^{\kappa_C \gamma_E}$ bandpowers with ACT+*Planck* tSZ-free κ_C and DES-Y3 shear, with four redshift bins. Error bars are the square root of the diagonal of the simulation covariance matrix, and z_{mean} is the mean redshift of the source galaxy distribution taken from (Abbott et al. 2022). The curves show the best fit theory $C_\ell^{\kappa_C \gamma_E}$ corresponding to best fit parameters in Table 3.
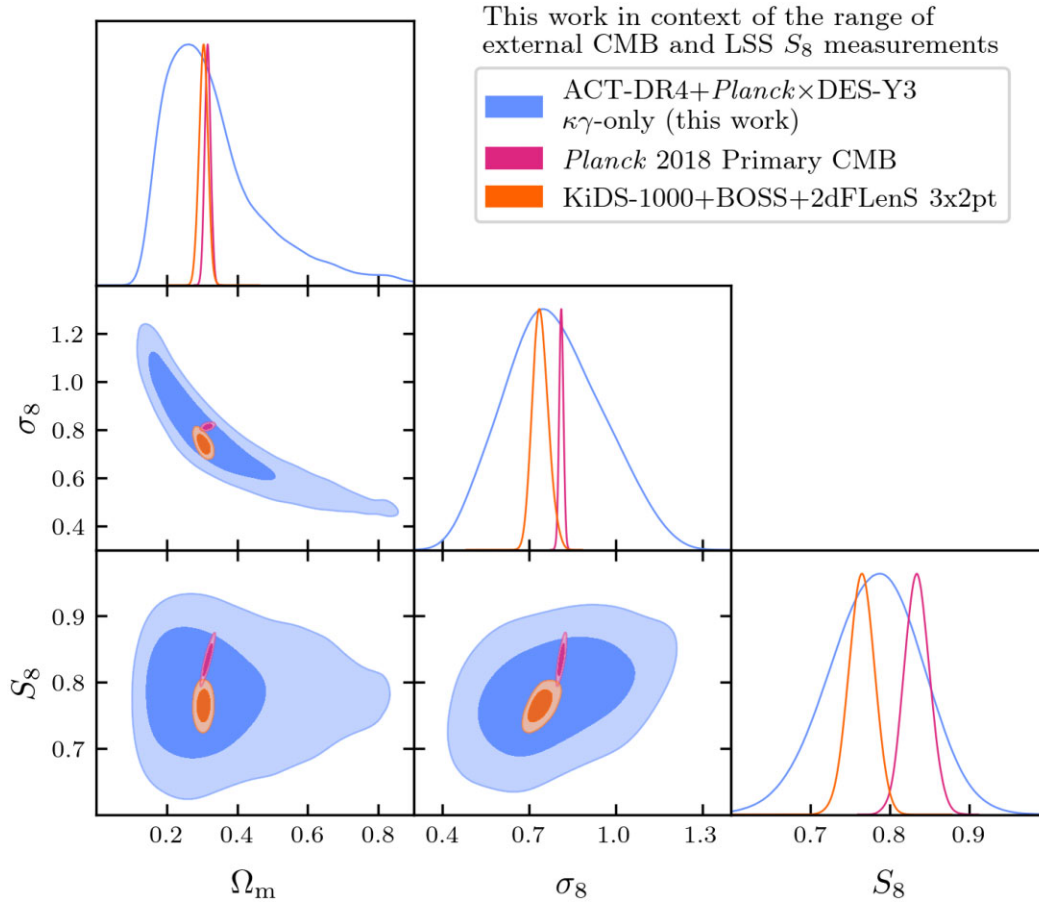
Figure 17. The inferred cosmological parameters σ_8, Ω_{m} and $S_8 = \sigma_8 (\Omega_{\mathrm{m}}/0.3)^{0.5}$ from our fiducial DES-Y3×ACT-DR4+*Planck*-tSZ deprojected data vector. To give context for our result, we also show results from other experiments with which we minimally share any data and cover the prominent range of S_8 values available in the literature. These are from the CMB at high redshift (*Planck* primary CMB) and LSS at lower redshifts (KiDS-1000+BOSS+2dFLenS 3×2pt). The full plot of this posterior, including nuisance parameters, is shown in Fig. B3.

the other contains only tomographic bins 3 and 4 (covering redshifts $0.63 < z < 2.0$ and with the resulting $C_\ell^{\kappa_C \gamma_E}$ kernel peaking above $z = 0.5$). In Fig. 19, we show the two posteriors on cosmological parameters, along with the one from our fiducial analysis with all four tomographic bins. For the sample at lower redshift (bins 1 and 2),

we obtained $\Omega_{\mathrm{m}} = 0.385^{+0.073}_{-0.22}$ and $S_8 = 0.85^{+0.17}_{-0.13}$, $\sigma_8 = 0.80^{+0.19}_{-0.23}$. Consistently, for the sample at higher redshift (bins 3 and 4), we found $\Omega_{\mathrm{m}} = 0.357^{+0.052}_{-0.20}$, $S_8 = 0.779 \pm 0.073$, $\sigma_8 = 0.77^{+0.15}_{-0.19}$. Our analysis reveals that the constraining power is significantly stronger at higher redshifts, primarily due to the better overlap with the CMB
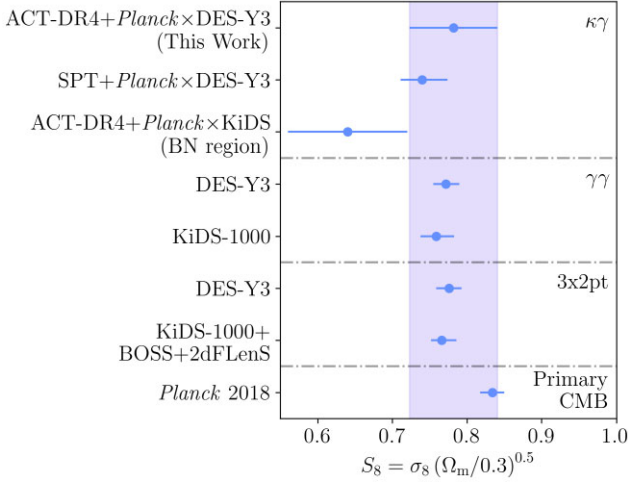
Figure 18. The measured cosmological parameter S_8 from our fiducial DES-Y3×ACT-DR4+*Planck*-tSZ deprojected data vector alongside a number of other measurements of the same parameters. Note that the ACT-DR4+*Planck*×KiDS measurement uses the κ_C of the BN region of ACT-DR4 data (Robertson et al. 2021).

Table 3. 1D Marginalized posterior mean and 68 per cent credible interval for the parameters sampled during our main analysis.

Parameter	Prior	Posterior
Cosmology		
$\Omega_c h^2$	$\mathcal{U}[0.05, 0.99]$	$0.161^{+0.042}_{-0.073}$
$\log(A_s 10^{10})$	$\mathcal{U}[1.6, 4.0]$	—
H_0	$\mathcal{U}[40, 100]$	—
σ_8	—	$0.79^{+0.16}_{-0.19}$
Ω_m	—	$0.338^{+0.05}_{-0.17}$
$S_8 = \sigma_8(\Omega_m/0.3)^{0.5}$	—	0.782 ± 0.059
Galaxy IA		
A_{IA}	$\mathcal{N}(0.35, 0.65)$	0.31 ± 0.57
η_{IA}	$\mathcal{N}(1.66, 4)$	$-1.0^{+3.8}_{-3.1}$
Galaxy redshift calibration		
Δz_1	$\mathcal{N}(0.0, 0.018)$	0.001 ± 0.018
Δz_2	$\mathcal{N}(0.0, 0.015)$	0.001 ± 0.015
Δz_3	$\mathcal{N}(0.0, 0.011)$	-0.001 ± 0.011
Δz_4	$\mathcal{N}(0.0, 0.017)$	0.000 ± 0.017
Galaxy shear calibration		
m_1	$\mathcal{N}(-0.006, 0.009)$	-0.0062 ± 0.0089
m_2	$\mathcal{N}(-0.020, 0.008)$	-0.0198 ± 0.0080
m_3	$\mathcal{N}(-0.024, 0.008)$	-0.0240 ± 0.0080
m_4	$\mathcal{N}(-0.037, 0.008)$	-0.0370 ± 0.0080

lensing kernel. This suggests that the dominant contribution to the overall constraining power when utilizing the entire sample stems from these bins.

7.4 Weak lensing nuisance parameters

The priors on weak lensing galaxy redshift and shear calibration detailed in Table 2 and used in the above inference runs are derived from a series of simulations and deep training data implemented as part of the DES-Y3 analysis pipelines. They are therefore informative and dominate the posterior for the nuisance parameters (as seen in Appendix Fig. B2). It is interesting to use the CMB lensing from ACT-DR4 as an extra high redshift lensing bin to attempt
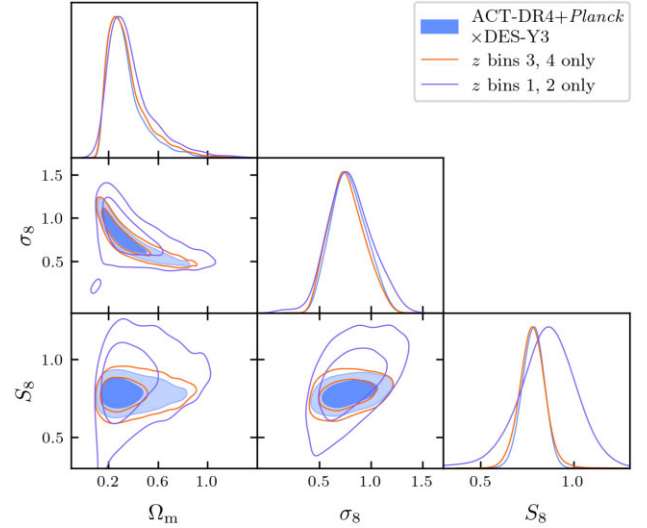
Figure 19. Measurement of the cosmological parameters in two subsets of the data, one covering galaxy redshifts $0 < z \leq 0.63$ and with the resulting $C_\ell^{\kappa_C \gamma_E}$ kernel peaking below $z = 0.5$ and the other covering redshifts $0.63 < z < 2.0$ and with the resulting $C_\ell^{\kappa_C \gamma_E}$ kernel peaking above $z = 0.5$. We find both subsets of the inferred parameters to be consistent.

to independently calibrate these nuisance parameters and validate the priors available from simulations. This has been previously advocated as a productive use of $C_\ell^{\kappa_C \gamma_E}$ data sets (e.g. Das, Errard & Spergel 2013). Though these simulation-derived priors are often given as uncorrelated, wider priors may result in degeneracies in 3×2pt analyses. In such a case, the $C_\ell^{\kappa_C \gamma_E}$ observable may provide useful degeneracy breaking thanks to the differences in redshift and scale dependence. Here, we make use of only the highest redshift and highest signal tomographic bin (Bin 4), fix all other cosmological and nuisance parameters to their fiducial values and infer only the redshift and shear calibration parameters (δz_4, m_4) with broad priors $\delta z_4 \sim \mathcal{U}[-1, 2]$ and $m_4 \sim \mathcal{U}[-1, 1]$. These priors are a factor 100 wider than the Gaussian priors applied in the main analysis and span the plausible range of possible calibration uncertainties. The inferred posterior is shown in Fig. 20. Though the constraining power of our data is far lower than that of the DES-Y3 prior, the posterior is consistent, meaning the informative prior passes as accurate within the terms of this low precision test.

8 CONCLUSIONS

In this analysis, we measured $C_\ell^{\kappa_C \gamma_E}$, the angular power spectrum between the CMB weak lensing map of ACT-DR4 in the D56 region and the DES-Y3 cosmic shear catalogue consisting of around 100 million galaxies. The measurement is over the common sky area of around 450 deg^2 between the two surveys. To avoid one of the main extragalactic foreground biases which originate from the tSZ contamination in κ_C, we used the tSZ-free κ_C map obtained using ACT-DR4 and *Planck* data for the baseline analysis (Darwish et al. 2021). The analysis is carried out in harmonic space over the multipole range of $\ell = 100$ to 1900. Over this range, we measure the cross-correlation at SNR = 7.1. As demonstrated in Section 6.1, the measured data vector passes specific null tests, indicating the lack of significant detection of some of the non-idealities that generally affect $C_\ell^{\kappa_C \gamma_E}$ measurements. We also tested for contamination due to stars and Galactic dust. We found their effect is negligible compared with the statistical uncertainty and saw no significant evidence of their
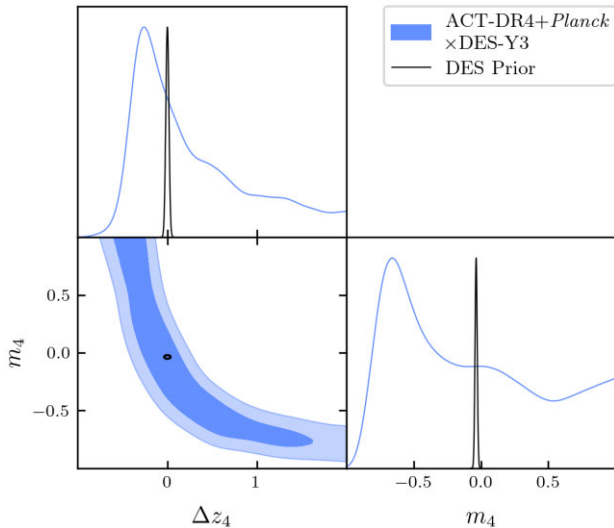
Figure 20. Constraints on the galaxy weak lensing nuisance parameters in DES-Y3 tomographic bin 4 ($0.87 < z < 2.0$). The DES-Y3 prior used in the main analysis is shown as unfilled contours and is consistent with the filled contours obtained with fixed cosmological parameters but broad priors on nuisance parameters.

contamination. We performed the initial analysis with the blinding procedure described in Section 3.2.1. After the data vector passed the null tests and we confirmed that the analysis pipeline recovered the unbiased input values from simulations, we unblinded the catalogue and the parameters inferred from the unblinded data vector.

We used this $C_\ell^{\kappa_C \gamma_E}$ measurement to infer the matter density parameter (Ω_m) and the amplitude of fluctuations in the matter distribution (S_8). We inferred $\Omega_m = 0.338^{+0.05}_{-0.17}$, and $S_8 = 0.782 \pm 0.059$. Our main result is shown in Fig. 17. These values were inferred using informative but well motivated priors on the observational and astrophysical nuisance parameters, which were marginalized while inferring Ω_m and S_8. We investigated the validity of the priors on galaxy IA parameters by significantly relaxing them and checking the consistency of the resulting posteriors. As depicted in Fig. 13, we found the posteriors with this broader IA prior are consistent with those with the fiducial IA priors but have relatively weak constraints on the cosmological parameters. We also assessed the consistency between the inference obtained using various subsets of the data, shown in Fig. 19. Our results are statistically consistent with many recent cosmic shear studies, including those utilizing the DES-Y3 data alone (Abbott et al. 2022; Doux et al. 2022, Secco et al. 2022, Amon et al. 2022) and cross-correlation with SPT and *Planck* CMB lensing (Chang et al. 2023). Furthermore, our results are in agreement with S_8 inferred using KiDS data (Heymans et al. 2021), although slightly higher than the value inferred using the cross-correlation with ACT-DR4 BOSS North and *Planck* CMB lensing (Robertson et al. 2021). However, we note that these differences fall within $\sim 1.4\sigma$, indicating a relatively minor deviation. We summarized this comparison in Fig. 18.

Measurements of the clustering of matter from combinations of CMB and optical weak lensing are rapidly growing in precision, with the highest-yet SNR achieved being that of SPT+*Planck*×DES-Y3 at 18σ (Chang et al. 2023). We note that this analysis is carried out on a substantially larger sky area of 3920 deg^2 than the 450 deg^2 area of the ACT D56 region considered in this work. For a given sky area, comparatively higher SNR obtained in this work is owing to the lower κ_C reconstruction noise of the ACT D56 observations. We

find the S_8 inferred in these two studies in statistical agreement, as depicted in Fig. 18. Recently, the ACT Collaboration has completed an analysis of the reconstructed CMB lensing map using the DR6 sky area of 9400 deg^2, which overlaps with nearly the entire DES-Y3 survey footprint (MacCrann et al. 2023; Madhavacheril et al. 2023; Qu et al. 2023). These data will provide a great opportunity to continue the work done here by performing cross-correlation with various probes of LSS, including galaxy lensing and galaxy density (Marques et al. 2023). Further on the horizon, correlations between the Simons Observatory (Ade et al. 2019) and CMB-S4 (Abazajian et al. 2016) lensing maps with shear data from the *Euclid* satellite (Amendola et al. 2018) and the Rubin Observatory Legacy Survey of Space and Time (Ivezić et al. 2019) will be even more precise. These analyses, with their higher statistical precision, will need to be carried out with more careful theoretical modelling of astrophysical effects of baryons and galaxy IA along with the modelling of observational systematics (see, e.g. DES Collaboration & KiDS Collaboration 2023) than required for the data analysed in this work.

9 DATA AVAILABILITY

The data underlying this article are available in a GitHub repository at https://github.com/itrharrison/actdr4kappa-x-desy3gamma-data, in the Zenodo repository https://zenodo.org/records/8346047, and has been made available on the LAMBDA data service at https://lambda.gsfc.nasa.gov/product/act/actpol_prod_table.html.

REFERENCES

Abazajian K. N. et al., 2016, preprint (arXiv:1610.02743)
Abbott T. M. C. et al., 2018, Phys. Rev. D, 98, 043526
Abbott T. M. C. et al., 2021, ApJS, 255, 20
Abbott T. M. C. et al., 2022, Phys. Rev. D, 105, 023520
Abbott T. M. C. et al., 2023, Phys. Rev. D, 107, 023531
Abdalla E. et al., 2022, Journal of High Energy Astrophysics, 34, 49
Ade P. et al., 2019, JCAP, 2019, 056
Aiola S. et al., 2020, JCAP, 2020, 047
Alonso D., Sanchez J., Slosar A., LSST Dark Energy Science Collaboration, 2019, MNRAS, 484, 4127
Amendola L. et al., 2018, Living Reviews in Relativity, 21, 2
Amon A., Efstathiou G., 2022, MNRAS, 516, 5355
Amon A. et al., 2022, Phys. Rev. D, 105, 023514
Amon A. et al., 2023, MNRAS, 518, 477
Anderson T. W., 2003, An Introduction to Multivariate Statistical Analysis, 3rd edn. Wiley-Interscience, Hoboken, NJ
Asgari M. et al., 2021, A&A, 645, 104
Baxter E. J. et al., 2019, Phys. Rev. D, 99, 023508
Bridle S., King L., 2007, New Journal of Physics, 9, 444
Calabrese E., Slosar A., Melchiorri A., Smoot G. F., Zahn O., 2008, Phys. Rev. D, 77, 123531
Castro P. G., Heavens A. F., Kitching T. D., 2005, Phys. Rev. D, 72, 023516
Chang C. et al., 2023, Phys. Rev. D, 107, 023530
Chisari N. E. et al., 2019, ApJS, 242, 2
Choi S. K. et al., 2020, JCAP, 2020, 045
Cordero J. P. et al., 2022, MNRAS, 511, 2170
DES Collaboration, Kilo-Degree Survey Collaboration, 2023, The Open Journal of Astrophysics, 6, 36
Darwish O. et al., 2021, MNRAS, 500, 2250
Das S., Errard J., Spergel D., 2013, preprint (arXiv:1311.2338)
Doux C. et al., 2022, MNRAS, 515, 1942
Dutcher D. et al., 2021, Phys. Rev. D, 104, 022003
Favole G., Granett B. R., Silva Lafaurie J., Sapone D., 2021, MNRAS, 505, 5833
Flaugher B. et al., 2015, AJ, 150, 150
Friedrich O. et al., 2018, Phys. Rev. D, 98, 023508
Friedrich O. et al., 2021, MNRAS, 508, 3125
Gatti M. et al., 2021, MNRAS, 504, 4312
Górski K. M., Hivon E., Banday A. J., Wandelt B. D., Hansen F. K., Reinecke M., Bartelmann M., 2005, ApJ, 622, L759
Gu S., Dor M.-A., van Waerbeke L., Asgari M., Mead A., Tröster T., Yan Z., 2023, MNRAS, 525, 4871
Hall A., Taylor A., 2014, MNRAS, 443, 119
Hand N. et al., 2015, Phys. Rev. D, 91, 062001
Harnois-Déraps J. et al., 2016, MNRAS, 460, 434
Harnois-Déraps J. et al., 2017, MNRAS, 471, 1619
Hartlap J., Simon P., Schneider P., 2007, A&A, 464, 399
Hartley W. G. et al., 2022, MNRAS, 509, 3547
Heymans C. et al., 2006, MNRAS, 368, 1323
Heymans C. et al., 2021, A&A, 646, 140
Hikage C., Takada M., Hamana T., Spergel D., 2011, MNRAS, 412, 65
Hilbert S., Hartlap J., Schneider P., 2011, A&A, 536, 85
Hirata C. M., Mandelbaum R., Ishak M., Seljak U., Nichol R., Pimbblet K. A., Ross N. P., Wake D., 2007, MNRAS, 381, 1197
Hivon E., Górski K. M., Netterfield C. B., Crill B. P., Prunet S., Hansen F., 2002, ApJ, 567, L2
Howlett C., Lewis A., Hall A., Challinor A., 2012, J. Cosmology Astropart. Phys., 2012, 027
Hu W., Okamoto T., 2002, ApJ, 574, L566
Huff E., Mandelbaum R., 2017, preprint (arXiv:1702.02600)
Huterer D., Takada M., Bernstein G., Jain B., 2006, MNRAS, 366, 101
Ivezić Ž. et al., 2019, ApJ, 873, L111
Johnston H. et al., 2019, A&A, 624, 30
Kaiser N., 1992, ApJ, 388, L272
Kirk D. et al., 2016, MNRAS, 459, 21

Kitching T. D., Deshpande A. C., Taylor P. L., 2020, The Open Journal of Astrophysics, 3, 14

Krolewski A., Ferraro S., White M., 2021, JCAP, 2021, 028

Lewis A., 2013, Phys. Rev. D, 87, 103529

Lewis A., Bridle S., 2002, Phys. Rev. D, 66, 103511

Lewis A., Challinor A., Lasenby A., 2000, ApJ, 538, L473

Lewis A. et al., 2022, cmbant/CAMB: 1.3.5, Zenodo, available at: https://doi.org/10.5281/zenodo.6137931

Limber D. N., 1953, ApJ, 117, L134

Liu J., Hill J. C., 2015, Phys. Rev. D, 92, 063517

LoVerde M., Afshordi N., 2008, Phys. Rev. D, 78, 123506

MacCrann N. et al., 2022, MNRAS, 509, 3371

MacCrann N. et al., 2023, preprint (arXiv:2304.05196)

Madhavacheril M. S., Hill J. C., 2018, Phys. Rev. D, 98, 023534

Madhavacheril M. S. et al., 2020, Phys. Rev. D, 102, 023534

Madhavacheril M. S. et al., 2023, preprint (arXiv:2304.05203)

Mallaby-Kay M. et al., 2021, ApJS, 255, 11

Marques G. A., Liu J., Huffenberger K. M., Colin Hill J., 2020, ApJ, 904, L182

Marques G. A. et al., 2024, JCAP, 2024, 033

Mead A. J., Peacock J. A., Heymans C., Joudaki S., Heavens A. F., 2015, MNRAS, 454, 1958

Miyatake H. et al., 2023, Phys. Rev. D, 108, 123517

More S. et al., 2023, Phys. Rev. D, 108, 123520

Myles J. et al., 2021, MNRAS, 505, 4249

Namikawa T. et al., 2019, ApJ, 882, L62

Nicola A., García-García C., Alonso D., Dunkley J., Ferreira P. G., Slosar A., Spergel D. N., 2021, JCAP, 2021, 067

Norberg P., Baugh C. M., Gaztañaga E., Croton D. J., 2009, MNRAS, 396, 19

Omori Y. et al., 2019, Phys. Rev. D, 100, 043501

Omori Y. et al., 2023, Phys. Rev. D, 107, 023529

Osborne S. J., Hanson D., Doré O., 2014, JCAP, 2014, 024

Planck Collaboration, 2020, A&A, 641, 6

Poulin V., Bernal J. L., Kovetz E. D., Kamionkowski M., 2023, Phys. Rev. D, 107, 123538

Qu F. J. et al., 2023, preprint (arXiv:2304.05202)

Robertson N. C. et al., 2021, A&A, 649, 146

Rogers K. K., Hložek R., Laguë A., Ivanov M. M., Philcox O. H. E., Cabass G., Akitsu K., Marsh D. J. E., 2023, JCAP, 2023, 023

Samuroff S. et al., 2019, MNRAS, 489, 5453

Samuroff S. et al., 2023, MNRAS, 524, 2195

Sánchez C. et al., 2023, MNRAS, 525, 3896

Schlegel D. J., Finkbeiner D. P., Davis M., 1998, ApJ, 500, L525

Schmidt S. J., Ménard B., Scranton R., Morrison C. B., Rahman M., Hopkins A. M., 2015, MNRAS, 446, 2696

Schneider P., 2005, preprint (arXiv:astro-ph/0509252)

Secco L. F. et al., 2022, Phys. Rev. D, 105, 023515

Sevilla-Noarbe I. et al., 2021, ApJS, 254, 24

Sheldon E. S., Huff E. M., 2017, ApJ, 841, L24

Singh S., Mandelbaum R., Brownstein J. R., 2017, MNRAS, 464, 2120

Smith R. E. et al., 2003, MNRAS, 341, 1311

Sugiyama S. et al., 2023, Phys. Rev. D, 108, 123521

Takahashi R., Sato M., Nishimichi T., Taruya A., Oguri M., 2012, ApJ, 761, L152

Torrado J., Lewis A., 2019, Astrophysics Source Code Library, record ascl:1910.019

Torrado J., Lewis A., 2021, JCAP, 2021, 057

Troxel M. A., Ishak M., 2015, Phys. Rep., 558, 1

Vlah Z., Chisari N. E., Schmidt F., 2020, JCAP, 2020, 025

Xavier H. S., Abdalla F. B., Joachimi B., 2016, MNRAS, 459, 3693

van Engelen A., Bhattacharya S., Sehgal N., Holder G. P., Zahn O., Nagai D., 2014, ApJ, 786, L13

Yao J. et al., 2023, A&A, 673, 111

APPENDIX A: RESULTS WITH ACT-ONLY DATA VECTOR

We also perform all of our analysis with the $C_\ell^{\kappa_C \gamma_E}$ data vector containing only ACT-DR4 data (i.e. no *Planck* data and no tSZ deprojection). Fig. A1 shows the ACT-only data vector and the best fit $C_\ell^{\kappa_C \gamma_E}$. With ACT-only κ_C, we measure $C_\ell^{\kappa_C \gamma_E}$ at the SNR of 6.6, which is slightly less than the ACT+*Planck* SNR = 7.1. ACT-only $C_\ell^{\kappa_C \gamma_E}$ passes the null tests similar to the ACT+*Planck* $C_\ell^{\kappa_C \gamma_E}$ with PTE = 0.67 for the B-mode null test and PTE = 0.43 for the rotation null test. The null test bandpowers are depicted in Fig. A2.
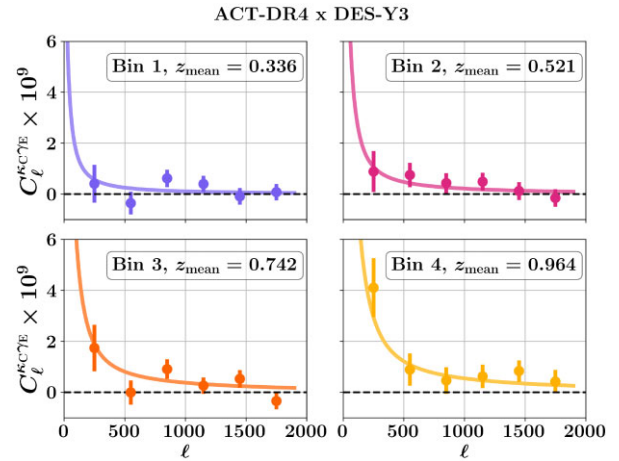

Figure A1. Similar to Section 7, but for ACT-only κ_C. The points with the error bar show $C_\ell^{\kappa_C \gamma_E}$ bandpowers with ACT-DR4 κ_C and DES-Y3 shear for four DES-Y3 redshift bins. Error bars are the square root of the diagonal of the covariance matrix. z_{mean} is the mean redshift of the source galaxy distribution. The curves show the best fit theory $C_\ell^{\kappa_C \gamma_E}$.
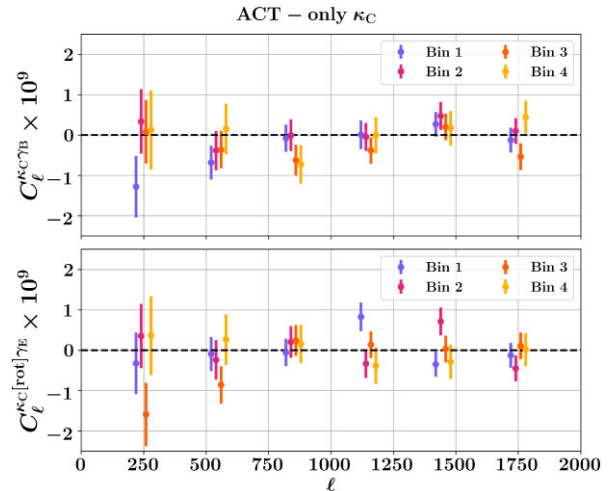

Figure A2. Similar to Fig. 10, but for ACT-only data. Top: The power spectrum between κ_C and the B-mode of the shear ($C_\ell^{\kappa_C \gamma_B}$), which is expected to be consistent with zero. Bottom: The correlation between κ_C and the E-mode of the shear map ($C_\ell^{\kappa_C [rot] \gamma_E}$) obtained from the catalogue in which ellipticities are randomly rotated.
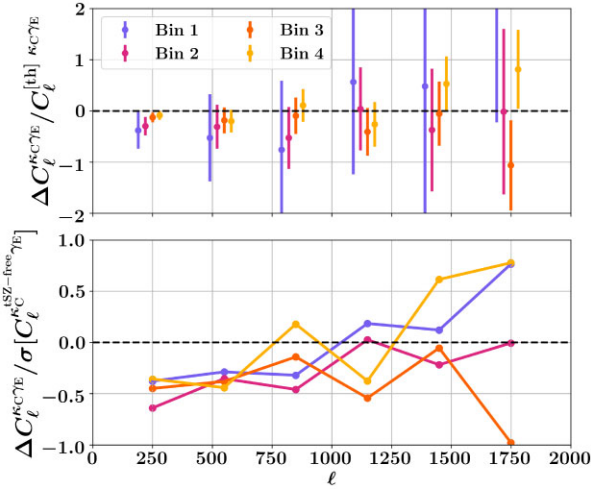
Figure A3. Comparison of $C_\ell^{\kappa_C \gamma_E}$ [ACT-only, with-tSZ] and $C_\ell^{\kappa_C \gamma_E}$ [ACT+*Planck*, tSZ-free]. Top: The difference between two ($\Delta C_\ell^{\kappa_C \gamma_E} \equiv C_\ell^{\mathrm{with-tSZ}} - C_\ell^{\mathrm{tSZ-free}}$) relative to the fiducial theory $C_\ell^{\kappa_C \gamma_E}$. The error bars depict $\sigma(\Delta C_\ell^{\kappa_C \gamma_E})/C_\ell^{[\mathrm{th}]\kappa_C \gamma_E}$, where $\sigma(\Delta C_\ell^{\kappa_C \gamma_E})$ is uncertainty on $\Delta C_\ell^{\kappa_C \gamma_E}$. Bottom: The same difference as in the top panel, $\Delta C_\ell^{\kappa_C \gamma_E}$, but now in units of error bar on tSZ-free $C_\ell^{\kappa_C \gamma_E}$.
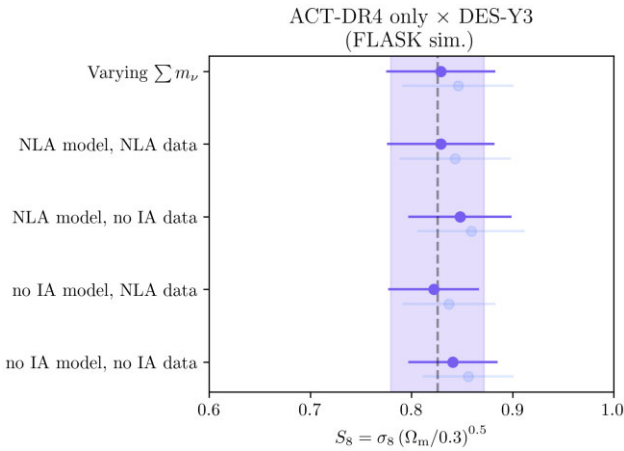

Figure A4. The stability of the recovery of the S_8 parameter from our simulated ACT-only data vector as we change the model used for the inference. Results from the fiducial ACT+*Planck* simulated data vector are shown as the faded points (and ACT-only results are not shown for all the model variations). The dashed vertical line represents the true value input to the simulation, and the shaded band is the error bar in the fiducial model setup.

A1 Comparison of ACT-only and ACT+*Planck* data vector

In this section, we compare $C_\ell^{\kappa_C \gamma_E}$ data vector obtained using ACT-only κ_C and ACT+*Planck* κ_C. An astrophysical systematic that is not modelled and is correlated with the reconstructed κ_C and galaxy shear can lead to a bias in the measurement of $C_\ell^{\kappa_C \gamma_E}$. In addition to the lensing, observed CMB maps contain the imprints of other secondary anisotropies and foregrounds, such as the Sunyaev–Zel'dovich effect and emissions from galaxies, such as the CIB. If these effects are sufficiently non-Gaussian over the scales of the CMB temperature anisotropies used to reconstruct κ_C, they can bias the lensing estimate. If, in addition, these secondary effects and extragalactic foregrounds share redshift overlap with a tracer
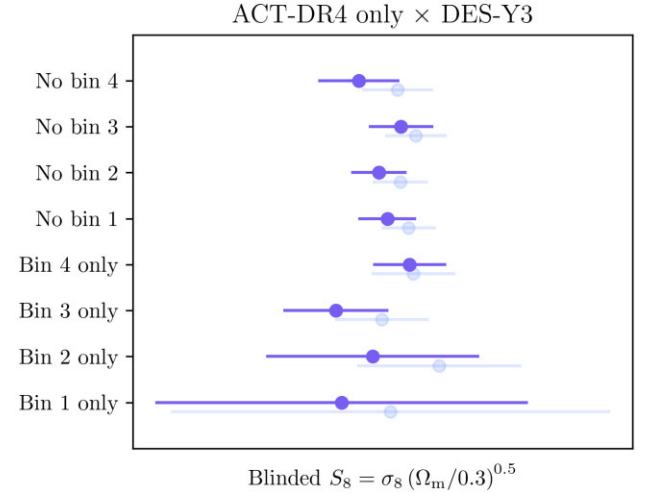

Figure A5. Stability of our 1D marginalized measurement of S_8 when using different parts of the full ACT only data vector (results from the fiducial ACT+*Planck* data vector are shown as points with lighter shade). In each row, we either remove a single DES-Y3 tomographic bin or use the data from only one of the four DES-Y3 bins.

of LSS, the cross-correlation of the reconstructed κ_C with these tracers is biased (Osborne, Hanson & Doré 2014; van Engelen et al. 2014). For correlations with cosmic shear, the effect of the tSZ bias is shown to be more severe at lower redshift bins (Baxter et al. 2019). In κ_C reconstruction with ACT 98 and 150 GHz maps, tSZ contamination is mitigated by finding and masking massive clusters in the temperature maps. The clusters detected above signal-to-noise ratio = 5 are masked in frequency maps, and the masked regions are in painted. However, this procedure does not remove all of the tSZ bias in the reconstructed κ_C. Hence, along with the ACT 98 and 150 GHz maps, Darwish et al. (2021) use *Planck* frequency maps from 30 to 545 GHz to deproject tSZ and reconstruct κ_C where the effect of tSZ is nulled. In Fig. A3, we show the difference between the $C_\ell^{\kappa_C \gamma_E}$ bandpowers for κ_C with ACT-only data and the ACT+*Planck* tSZ-free (which is our choice for the baseline analysis). We find that the four bandpowers are consistent with the hypothesis of no difference, with the PTEs for four redshift bin bandpowers being 0.86, 0.72, 0.68, and 0.65, respectively.

A2 Analysis results

The parameter inference with ACT-only $C_\ell^{\kappa_C \gamma_E}$ is performed with identical modelling choices as that of ACT+*Planck* $C_\ell^{\kappa_C \gamma_E}$. Fig. A4 shows the results with simulations of ACT-only $C_\ell^{\kappa_C \gamma_E}$ indicating the stability of recovery of the S_8 parameter for different models used for inference. Fig. A5 shows the consistency of the S_8 inference for different data combinations similar to the case of ACT+*Planck* as depicted by points with the lighter shade. We show the posterior distribution of the cosmological parameters in Fig. A6. We find that the σ_8 and S_8 inferred with ACT-only $C_\ell^{\kappa_C \gamma_E}$ are somewhat smaller than those inferred from ACT+*Planck* $C_\ell^{\kappa_C \gamma_E}$. This is consistent with what we observe in Fig. A3. ACT-only $C_\ell^{\kappa_C \gamma_E}$ has a smaller amplitude than ACT+*Planck* $C_\ell^{\kappa_C \gamma_E}$ at lower multiples, which are multipole bins with higher SNR, resulting in lower S_8 inference. The constraints on the shear calibration and photometric uncertainty parameters are similar to those obtained with ACT-only κ_C shown in Fig. A7.
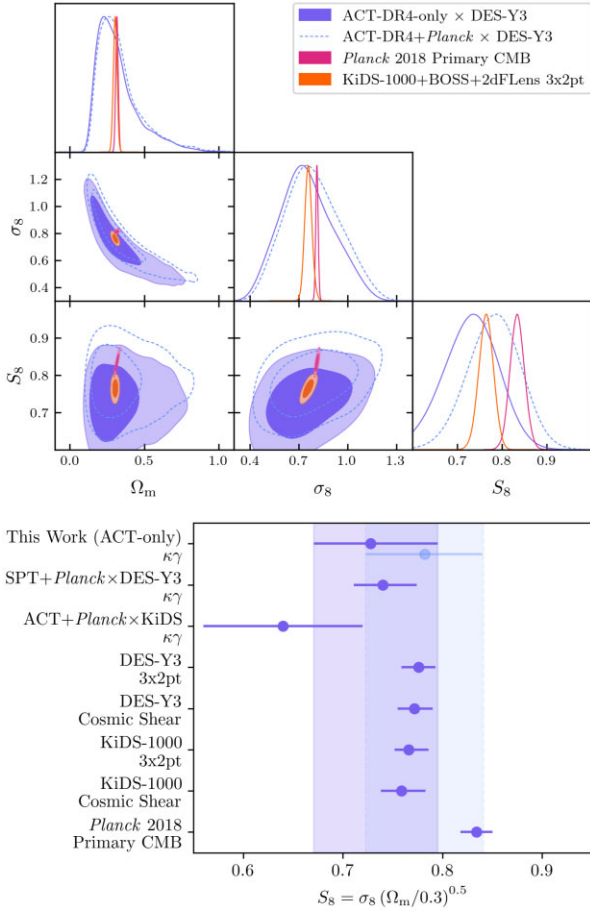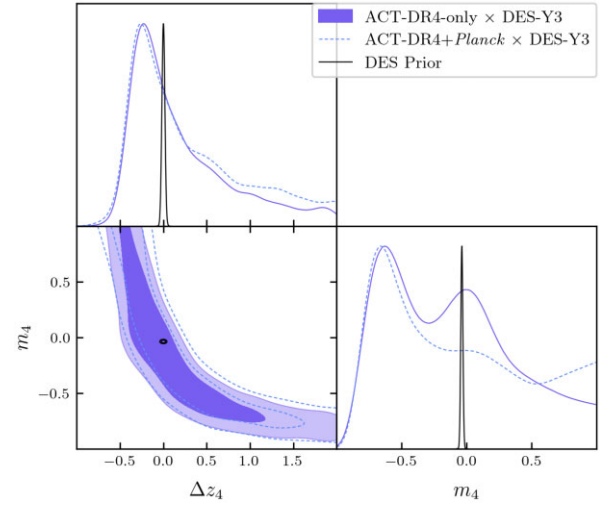
Figure A7. Constraints on the galaxy weak lensing nuisance parameters in DES-Y3 tomographic bin 4 ($0.87 < z < 2.0$) from ACT-only data vector (the result from the fiducial ACT+*Planck* data vector is shown as the dashed contour). The DES-Y3 prior used in the main analysis is shown as unfilled contours; note the consistency with the filled contours obtained with fixed cosmological parameters but broad priors on nuisance parameters.

Figure A6. Top: The inferred distribution of cosmological parameters Ω_m, σ_8, S_8 from our ACT-only $C_\ell^{\kappa_C \gamma_E}$ data vector alongside two other measurements (the result from the fiducial ACT+*Planck* data vector is shown as unfilled dashed contours). The ACT-only posterior has $S_8 = 0.728^{+0.067}_{-0.057}$. Bottom: ACT-only S_8 alongside a number of other measurements (with the result from the fiducial ACT+*Planck* data vector shown in a lighter shade). Note that the ACT+*Planck*×KiDS measurement uses the κ_C of the BN region of ACT-DR4 data (Robertson et al. 2021).

APPENDIX B: FURTHER ILLUSTRATIVE POSTERIOR PLOTS

In Figs B1 and B2, we present a complete version of the posterior shown in Fig. 13 (for the simulated data vector), but in blocks of panels containing only cosmological parameters, galaxy IA parameters, and weak lensing nuisance parameters. When presented here, axis limits are changed in order to get a full view of the relevant prior distributions. In Fig. B3, we show the full posterior from our baseline analysis of the ACT+*Planck*×DES-Y3 data, a part of which is already shown in Fig. 17.

Figure B1. Recovery of input model parameters using our pipeline as described in Section 6 alongside the 68 per cent and 95 per cent contours of the prior (unfilled black contours). These are the same marginalized 1D and 2D posterior distributions shown in Fig. 13, but display only the cosmological parameters to increase the clarity of details.
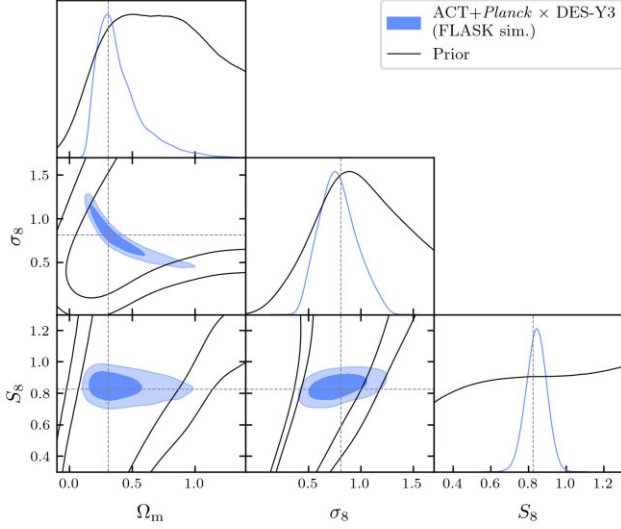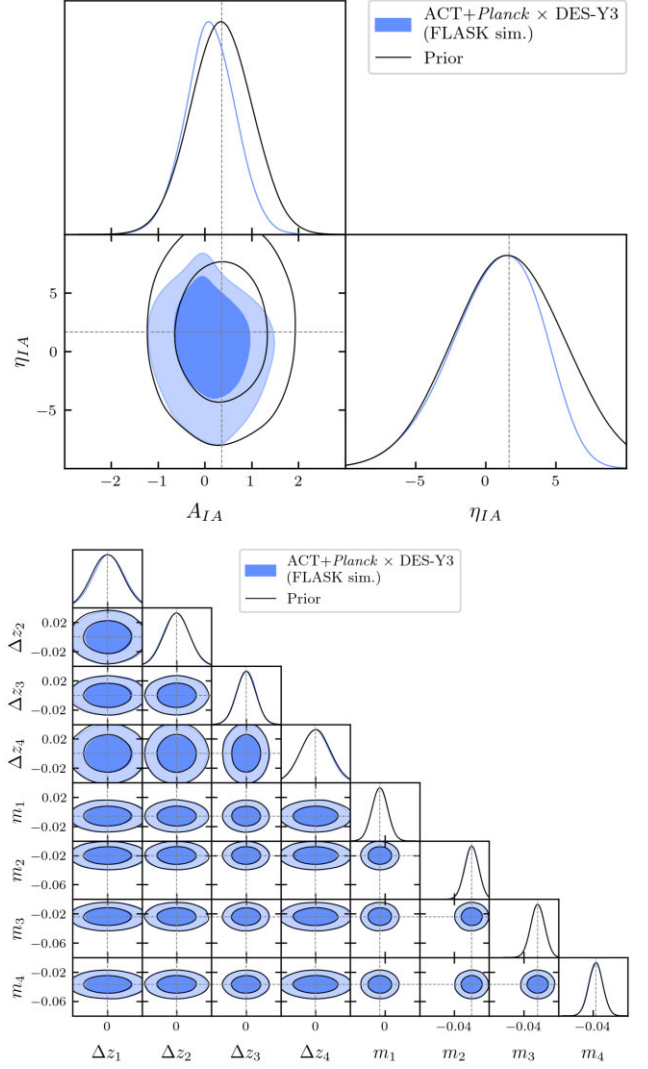

Figure B2. Recovery of input model parameters using our pipeline as described in Section 6 alongside the 68 per cent and 95 per cent contours of the prior (unfilled black contours). These are the same marginalized 1D and 2D posterior distributions shown in Fig. 13 but display only the IA parameters (top) and weak lensing nuisance parameters (bottom) to increase the clarity of details.
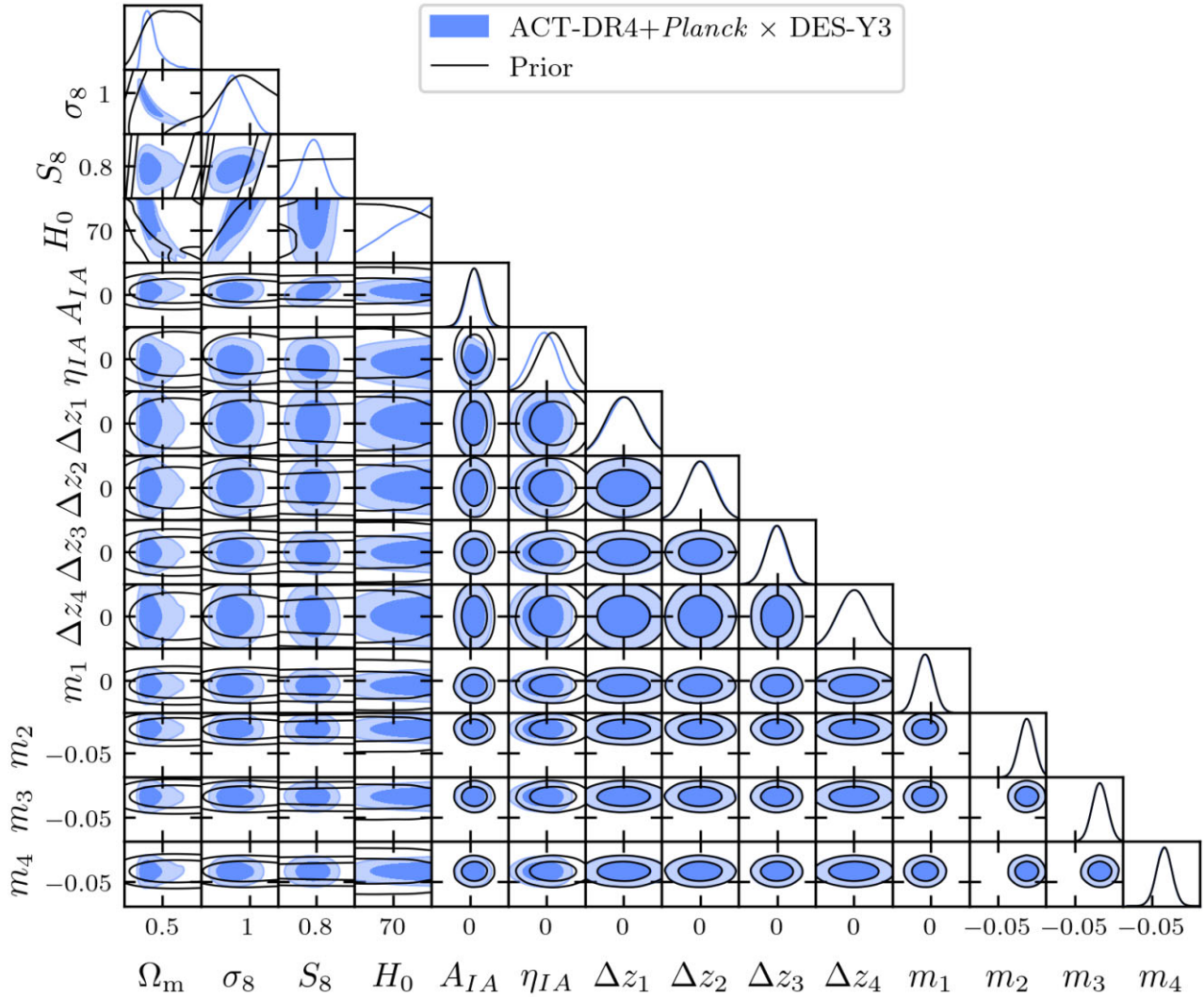
Figure B3. The full posterior from our baseline analysis is already shown in part in Fig. 17. Black unfilled contours show the priors specified in Table 2 as they appear in this output parameter space, and blue-filled contours show the recovered posterior constraints.

[1] *School of Earth and Space Exploration, Arizona State University, Tempe, AZ 85287, USA*

[2] *School of Physics and Astronomy, Cardiff University, CF24 3AA, UK*

[3] *Fermi National Accelerator Laboratory, P. O. Box 500, Batavia, IL 60510, USA*

[4] *Kavli Institute for Cosmological Physics, University of Chicago, Chicago, IL 60637, USA*

[5] *Cerro Tololo Inter-American Observatory, NSF's National Optical-Infrared Astronomy Research Laboratory, Casilla 603, La Serena, Chile*

[6] *Laboratório Interinstitucional de e-Astronomia – LIneA, Rua Gal. José Cristino 77, Rio de Janeiro, RJ - 20921-400, Brazil*

[7] *Department of Physics, University of Michigan, Ann Arbor, MI 48109, USA*

[8] *Institute of Astronomy, University of Cambridge, Madingley Road, Cambridge CB3 0HA, UK*

[9] *Kavli Institute for Cosmology, University of Cambridge, Madingley Road, Cambridge CB3 0HA, UK*

[10] *Department of Physics and Astronomy, University of Southern California, Los Angeles, CA 90089, USA*

[11] *Institute of Cosmology and Gravitation, University of Portsmouth, Portsmouth, PO1 3FX, UK*

[12] *Department of Astronomy, Cornell University, Ithaca, NY 14853, USA*

[13] *Argonne National Laboratory, 9700 South Cass Avenue, Lemont, IL 60439, USA*

[14] *Department of Physics and Astronomy, University of Pennsylvania, Philadelphia, PA 19104, USA*

[15] *CNRS, UMR 7095, Institut d'Astrophysique de Paris, F-75014, Paris, France*

[16] *Sorbonne Universités, UPMC Univ Paris 06, UMR 7095, Institut d'Astrophysique de Paris, F-75014, Paris, France*

[17] *Department of Physics, Northeastern University, Boston, MA 02115, USA*

[18] *Canadian Institute for Theoretical Astrophysics, University of Toronto, 60 St. George Street, Toronto, ON, M5S 3H8, Canada*

[19] *Department of Physics & Astronomy, University College London, Gower Street, London, WC1E 6BT, UK*

[20] *Kavli Institute for Particle Astrophysics & Cosmology, Stanford University, P. O. Box 2450, Stanford, CA 94305, USA*

[21] *SLAC National Accelerator Laboratory, Menlo Park, CA 94025, USA*

[22] *Instituto de Astrofisica de Canarias, E-38205 La Laguna, Tenerife, Spain*

[23] *Dpto. Astrofísica, Universidad de La Laguna, E-38206 La Laguna, Tenerife, Spain*

[24] *Institut de Física d'Altes Energies (IFAE), The Barcelona Institute of Science and Technology, Campus UAB, E-08193 Bellaterra, Barcelona, Spain*

[25] *Physics Department, William Jewell College, Liberty, MO 64068, USA*

[26] *Department of Astronomy and Astrophysics, University of Chicago, Chicago, IL 60637, USA*

[27] *Department of Physics, Duke University Durham, NC 27708, USA*

[28]*NASA Goddard Space Flight Center, 8800 Greenbelt Rd, Greenbelt, MD 20771, USA*

[29]*Department of Physics, Cornell University, Ithaca, NY 14853, USA*

[30]*Hamburger Sternwarte, Universität Hamburg, Gojenbergsweg 112, 21029 Hamburg, Germany*

[31]*Département de Physique Théorique et CAP, Université de Genève, 24 quai Ernest-Ansermet, CH-1211 Genève 4, Switzerland*

[32]*School of Mathematics and Physics, University of Queensland, Brisbane, QLD 4072, Australia*

[33]*Department of Physics, IIT Hyderabad, Kandi, Telangana 502285, India*

[34]*Université Grenoble Alpes, CNRS, LPSC-IN2P3, F-38000 Grenoble, France*

[35]*Department of Physics and Astronomy, University of Waterloo, 200 University Avenue West, Waterloo, ON N2L 3G1, Canada*

[36]*Department of Applied Mathematics and Theoretical Physics, University of Cambridge, Cambridge CB3 0WA, UK*

[37]*Lawrence Berkeley National Laboratory, 1 Cyclotron Road, Berkeley, CA 94720, USA*

[38]*Berkeley Center for Cosmological Physics, Department of Physics, University of California, Berkeley, CA 94720, USA*

[39]*Institute of Theoretical Astrophysics, University of Oslo, P. O. Box 1029 Blindern, NO-0315 Oslo, Norway*

[40]*Instituto de Fisica Teorica UAM/CSIC, Universidad Autonoma de Madrid, E-28049 Madrid, Spain*

[41]*University Observatory, Faculty of Physics, Ludwig-Maximilians-Universität, Scheinerstr. 1, D-81679 Munich, Germany*

[42]*Center for Astrophysical Surveys, National Center for Supercomputing Applications, 1205 West Clark Street, Urbana, IL 61801, USA*

[43]*Department of Astronomy, University of Illinois at Urbana-Champaign, 1002 W. Green Street, Urbana, IL 61801, USA*

[44]*Department of Physics, Columbia University, 538 West 120th Street, NY 10027, USA*

[45]*Santa Cruz Institute for Particle Physics, Santa Cruz, CA 95064, USA*

[46]*Center for Cosmology and Astro-Particle Physics, The Ohio State University, Columbus, OH 43210, USA*

[47]*Department of Physics, The Ohio State University, Columbus, OH 43210, USA*

[48]*Department of Physics, Florida State University, Tallahassee, FL 32306, USA*

[49]*Center for Astrophysics | Harvard & Smithsonian, 60 Garden Street, Cambridge, MA 02138, USA*

[50]*Centre for Radio Astronomy Techniques and Technologies, Department of Physics and Electronics, Rhodes University, P. O. Box 94, Makhanda 6140, South Africa*

[51]*South African Radio Astronomy Observatory, 2 Fir Street, Observatory 7925, South Africa*

[52]*Jet Propulsion Laboratory, California Institute of Technology, 4800 Oak Grove Dr, Pasadena, CA 91109, USA*

[53]*Departamento de Física Matemática, Instituto de Física, Universidade de São Paulo, CP 66318, São Paulo, SP, 05314-970, Brazil*

[54]*George P. and Cynthia Woods Mitchell Institute for Fundamental Physics and Astronomy, and Department of Physics and Astronomy, Texas A&M University, College Station, TX 77843, USA*

[55]*Centro de Investigaciones Energéticas, Medioambientales y Tecnológicas (CIEMAT), Av. Complutense, 40, Moncloa - Aravaca, E-28040 Madrid, Spain*

[56]*Institució Catalana de Recerca i Estudis Avançats, E-08010 Barcelona, Spain*

[57]*Max Planck Institute for Extraterrestrial Physics, Giessenbachstrasse, D-85748 Garching, Germany*

[58]*Astrophysics Research Centre, University of KwaZulu-Natal, Westville Campus, Durban 4041, South Africa*

[59]*School of Mathematics, Statistics & Computer Science, University of KwaZulu-Natal, Westville Campus, Durban 4041, South Africa*

[60]*Department of Physics, Stanford University, 382 Via Pueblo Mall, Stanford, CA 94305, USA*

[61]*Instituto de Física Gleb Wataghin, Universidade Estadual de Campinas, 13083-859, Campinas, SP, Brazil*

[62]*Department of Physics, Yale University, 217 Prospect Street, New Haven, CT 06511, USA*

[63]*Department of Physics and Astronomy, Haverford College, Haverford, PA, 19041, USA*

[64]*Observatório Nacional, Rua Gal. José Cristino 77, Rio de Janeiro, RJ - 20921-400, Brazil*

[65]*Institute for Astronomy, University of Edinburgh, Edinburgh EH9 3HJ, UK*

[66]*Department of Physics and Astronomy, Stony Brook University, Stony Brook, NY 11794, USA*

[67]*Brookhaven National Laboratory, Building 510, Upton, NY 11973, USA*

[68]*Instituto de Física, Pontificia Universidad Católica de Valparaíso, Casilla 4059, Valparaíso, Chile*

[69]*School of Physics and Astronomy, University of Southampton, Southampton, SO17 1BJ, UK*

[70]*Computer Science and Mathematics Division, Oak Ridge National Laboratory, Oak Ridge, TN 37831, USA*

[71]*Institut de Recherche en Astrophysique et Planétologie (IRAP), Université de Toulouse, CNRS, UPS, CNES, 14 Avenue Edouard Belin, F-31400 Toulouse, France*

[72]*Instituto de Astrofísica and Centro de Astro-Ingenieía, Facultad de Física, Pontificia Universidad Católica de Chile, Avenida Vicuña Mackenna 4860, 7820436 Macul, Santiago, Chile*

This paper has been typeset from a TEX/LATEX file prepared by the author.